Structural Design and Analysis of a Kinematic Mechanism for a Morphing Hyper-Elliptic Cambered Span (HECS) Wing

by

Leonard D. Wiggins, III

Thesis Submitted to the Faculty of the
Virginia Polytechnic Institute and State University
in partial fulfillment of the requirements for the degree of

Master of Science

in

Mechanical Engineering

Dr. Harry H. Robertshaw, Chair
Dr. Charles F. Reinholtz
Dr. Robert L. West
Dr. Daniel J. Inman

December 17, 2003

Blacksburg, Virginia

Keywords: morphing wing, HECS wing, kinematics, structural analysis, FEA

Structural Design and Analysis of a Kinematic Mechanism for a Morphing Hyper-Elliptic Cambered Span (HECS) Wing

Leonard D. Wiggins, III

(ABSTRACT)

The HECS wing was developed by NASA Langley Research Center and has a nonplanar, hyper-elliptically swept leading and trailing edge as well as spanwise camber. For this wing, the leading and trailing edges are swept back according to a hyper-elliptical equation. The span of the wing is also defined with hyper-elliptical anhedral giving it nonplanar spanwise camber. A single-degree-of-freedom mechanism is developed to provide a means for the wing to continuously change shape from its nonplanar to planar configuration. The mechanism uses a repeating quaternary-binary link configuration to translate motion from one segment to the next. A synthesis of the mechanism is performed, such that with one input to the first segment of the chain, the other wing segments move into their desired positions. Linear aerodynamic theory is applied to the HECS wing configuration at certain morphed positions in order to predict the aerodynamic loads.

This work performs a linear static analysis of the mechanism at different morphed positions. A finite element representation of the mechanism as a structure is developed. Using the predicted aerodynamic loads, a structural analysis is performed. The analysis investigates different materials and cross sections of the members to determine a need for redesign due to failure from buckling and bending stress. From the analysis of the mechanism, a design is finalized which lightens the structure as well as increases the strength. These results are beneficial for the next phase of model development of the mechanism.

Acknowledgments

I would like to thank my advisor Dr. Harry H. Robertshaw for all of his support throughout this work. It has truly been a pleasure having your insight and guidance with this project and my graduate studies. I would also like to than Dr. Daniel J. Inman for his financial support and for his great sense of humor that always provides a laugh. To Dr. Charles F. Reinholtz, I would like to thank you for the hands on experience with building the kinematic models for this work and for inviting us over to the nice woodshop in his basement. Thanks also to Dr. Robert L. West for taking time to answer my finite element and ANSYS questions. I would like to acknowledge Dr. Lucas Horta at NASA Langley Research Center in Hampton, VA for funding and having the idea for this work. I would also like to thank my HECS team members Christopher O. Johnston, Matthew D. Stubbs, and William B. Whittier for their work on this project.

I would like to say thank you to my family and friends for all of their support and prayers throughout my undergraduate and graduate work as well. I would especially like to thank my mother Vivian A. Allmon, my stepfather David Allmon, and my sister Vakesia L. Graves for everything. I could not have made it this far without your love and support. Finally, to my friends and colleagues at CIMSS, I want to say thanks for answering my questions, providing advice, and for putting up with my silliness. I wish you all many blessings and the best of luck.

Table of Contents

List of Tables

List of Figures

Nomenclature

P_{cr} - Critical force

E - Young's modulus of elasticity

I - Area moment of inertia

k - Radius of gyration

S_r - Slenderness ratio

A - Area of cross section

L - Length of member

σ - Bending stress

M - applie Bending moment

c - Distance from neutral axis to top of beam

u - Global displacement in x direction

$\hat{u}$ - Local displacement in x direction

v - Global displacement in y direction

$\hat{v}$ - Local displacement in y direction

W - Global displacement in z direction

$\hat{w}$ - Local displacement in z direction

θ_z - Rotation about the z axis

P - Applied force in x direction

Q - Applied force in y direction

$[k]$ - Elemental stiffness matrix

$[T]$ - Transformation matrix

$[F]$ - Global force matrix

$[f]$ - Local force matrix

$[K]$ - Global siffness matrix

$[d]$ - Global displacements vector

b - Width of rectangular cross section

h - Height of rectangular cross

C - Constraint equation coefficient

L - Nodal degree-of-freedom

θ - Nodal rotational degree-or-freedom

Chapter 1

Introduction

1.1 Morphing Wing Background

Morphing wing technology deals with the shape change of an aircraft wing using continuous control surface changes and/or changes of the planform. These shape changes provide an improvement and/or new vehicle system performance during flight. The continuous shape change of an airfoil and wing control surface is often referred to as flight control morphing. A wing that changes planform shape is a type of mission adaptive morphing. Flight control and mission adaptive morphing are the two main techniques of morphing a wing. There are works that have studied the benefits and energy requirements of morphing wings.

Types of Wing Morphing

Flight control morphing differs from discrete changes used by conventional air vehicles such as flaps. Flight control morphing changes the shape of the airfoil of the wing through variable leading and trailing edge camber and twist. For different flight conditions, flight control morphing could be used to minimize drag and act as a more efficient type of aileron.

Most standard aircraft wings are currently at a disadvantage when needing to perform two different flight objectives such as cruise and attack. Planform morphing wings can utilize their change in shape to adapt to such distinctly different objectives. Some means of planform

morphing that have been investigated include variable sweep, span, and dihedral. For example, an aircraft with variable sweep can increase its sweep angle in order to enter attack mode.

Morphing Wing Literature Review

There is research and development that attempts to model and predict the energy requirements and potential benefits of air vehicles that feature morphing wing technology. Some of those findings include a model that was created to investigate the energy requirements of active materials (Pettit *et al*, 2001). A comparison of power requirements between morphing and conventional wings for rolling maneuvers was also performed (Gern *et al*, 2002). Another model was created that also compared morphing and conventional wings, but this comparison evaluated the flight control energy requirements (Johnston *et al*, 2003). An assessment of energy minimization for shape changing morphing airfoils was explored as well (Prock *et al*, 2002).

Pettit *et al* (2001) created a computational model which evaluated the energy requirements of active materials in morphing wings. The model developed had the ability to predict the force, stroke, and energy needed to overcome the aerodynamic forces encountered during flight. The model allowed for the wing shapes to be easily changed and determined. Pettit *et al*'s (2001) work also incorporated an aerodynamic model which calculated the air loads on the shape. The dynamics of the systems had three-degrees-of-freedom. The stroke, power, and energy requirements were determined for an arbitrary desired course which the user input into the model.

The power requirements of a morphing and conventional wing in rolling maneuvers were investigated in Gern *et al*'s (2002) work. The paper presented the possibility of increasing roll performance of a wing by using a distributed surface rather than a conventional wing with trailing edge flaps. Gern *et al* (2002) found that using morphing airfoils offered the potential to increase the performance of an air vehicle. Since the maximum roll performance for different actuation schemes occurs at different flight speeds, it was proposed that the flight controller be changed while maintaining a constant structural setup. This would have tailored the roll reversal behavior of the morphing wing and also required the need for adaptive control laws that would be modified according to the flight conditions.

On the other hand, Johnston *et al* (2003) developed an analytical model that compared the predicted flight control energy requirements of morphing and conventionally actuated wings.

This was accomplished by using an adaptive camberline to generate the morphing wing shapes. The aerodynamic energy was derived from these camberline functions using a vortex lattice method. Strain energy expressions were obtained using beam theory on the morphing airfoil sections. Lagrange multipliers were used in combination with the aerodynamic and strain energies to obtain energy optimal deflections. With total energy as the cost functions and constraints on achieving lift and moment coefficients, work expressions for a wing with morphing inputs and a conventional wing, with inboard and outboard flaps, were executed numerically. The work concluded that although morphing vehicles generated strain energy not produced by conventional aircraft, the independent spanwise morphing deflection allowed for minimization of the aerodynamic energy requirements.

Prock *et al*'s (2002) work examined shape change optimization of morphing wing airfoils while wanting to minimize the actuation energy. The work explored a method of linking analytical models and optimization with design techniques to create energy efficient and lightweight wing structure and actuator combinations for morphing aircraft wings. The energy required to change from one wing shape to another was the guideline for optimization while aerodynamic performance was constrained. Three topics are discussed: the energy required to operate articulated trailing edge flaps and slats connected to flexible 2-D airfoils; lift generated using articulated, optimal, minimum energy wing control deflections; and strain energy changes required to go from one lift coefficient to another when wing cross-sectional shape was changed.

1.2 The Hyper –Elliptic Cambered Span (HECS) Wing

As part of its Morphing Project, NASA Langley Research Center (LaRC) developed the HECS wing configuration from its biologically inspired flight research. The wing consists of a hyper-elliptically swept leading and trailing edge as well as spanwise camber. The HECS wing design is illustrated in Figure 1.1. Its shape came from observations of the wings of shore birds during flapping flight. From wind tunnel tests conducted in the Basic Aerodynamics Research Tunnel at NASA LaRC, the HECS wing design shows an improvement by 14% in lift to drag ratio compared to a planar, elliptical chord wing with equal planform area and aspect ratio (McGowan *et al*, 2002). Literature which supports the experimental findings of the elliptical and cambered span type design is discussed in the next section. NASA LaRC is conducting research into morphing the HECS wing as well.

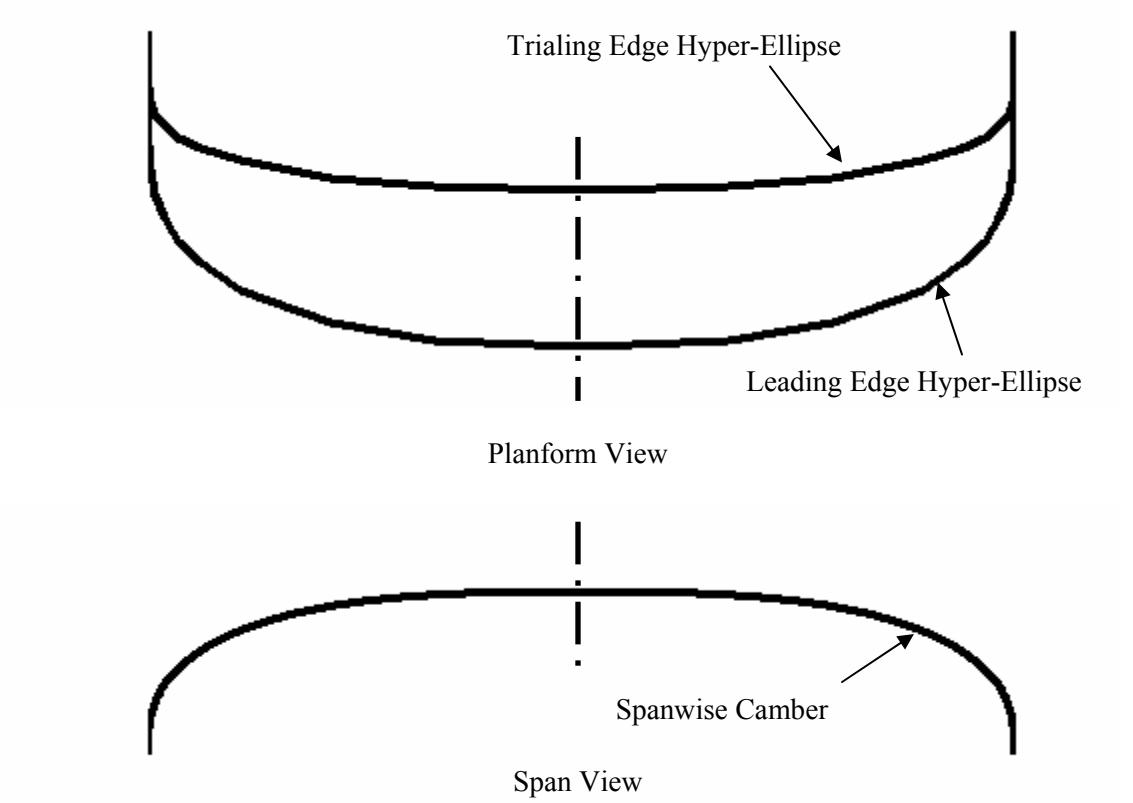

Figure 1.1: An illustration of the HECS wing design.

Elliptical and Cambered Span Wing Review

There is literature which investigated the elliptical and cambered span, nonplanar, wing configurations. Such works include a study that was conducted on the theory of induced lift and minimum induced drag of nonplanar surfaces (Cone, 1962). An exploration of the aerodynamic design of cambered span wings was performed also (Cone,1963). Another work took a computational approach to the effects of cambered span on induced drag (Lowson, 1990). These analyses showed benefits in the use of an elliptical and cambered span wing design.

Cone (1962) worked on the theory behind the induced lift and minimum induced drag of nonplanar lifting systems. The work presented the basic theoretical concepts and guidelines for determining the induced lift and minimum induced drag for nonplanar lifting systems. It was found that the induced drag efficiency can be expressed in terms of an effective aspect ratio. When those theoretical results were applied in order to predict the effective aspect ratio of lifting

surfaces with equal spans, it was discovered that reductions in induced drag were obtained by the use of nonplanar lifting surfaces. In particular, cambered span wings increased the effective aspect ratio by as much as 50 percent when compared to a flat, elliptical wing that generated equal lift and with equal span. It was also determined that the overall efficiency increase depended upon the structural weight and drag profile of the cambered system.

The aerodynamic design of cambered span wings with minimum induced drag was also examined by Cone (1963). Basic aerodynamic relations for wings having cambered span with minimum induced drag were determined. Also, methodologies were developed in order to determine the wing formation needed to maximize lift-to-drag ratio at cruise by optimizing chord and twist distributions related to profile and induced drag. When a cambered span wing and a flat wing with equal span were compared, the cambered span wing proved to be more efficient when the cambered design was made to minimize the profile drag of the wing. The improvements over optimal flat wings were found to be smaller at low lift coefficients because of the high proportion of profile drag. However, at higher lift coefficients, the induced drag is more prevalent and the higher effective aspect ratio of the cambered span wings was significant for limited wing spans.

Lowson (1990) performed a general study of the effects of a cambered span on induced drag. A computational approach which enabled better flexibility in the definition of the camberline was presented. This approach was in contrast to previous analytical approaches that did not have the camberline study ability. The work found that the benefits of optimum lift distributions for cambered lifting lines were in large part due to the camber at the wing tips. A wing with end plates was the most effective form of spanwise camber for a given maximum displacement, because of its vertical orientation. However, elliptic and superelliptic shapes were beneficial when the minimum length of wing for a given displacement was considered.

1.3 Morphing the HECS Wing

One of the goals of morphing the HECS wing is to have it change shape from its designed nonplanar position to a fully planar position. Figure 1.3 shows an illustration of the nonplanar and planar positions. A HECS wing with such variable dihedral would be a mission adaptive type morphing wing. Planform morphing can be advantageous for a flight vehicle with two different design objectives such as efficient cruise and high maneuverability. The main objective

when incorporating low speed efficient cruise is to minimize the induced drag. A wing with the largest possible span is ideal for this intention. Thus, in the case of a morphing HECS wing, the planar wing position is modeled. In order to maneuver at low lift coefficients, it is desirous to minimize the wing-root bending moment and maximize the obtainable roll-rate. The nonplanar position of the HECS wing meets this objective (Wiggins *et al*, 2004).

A morphing HECS wing also presents the capability of longitudinal and lateral-directional control. This can be accomplished not by necessarily varying the dihedral of the full wing, but by morphing the wing tips. The wing tips can be changed by varying twist or even some type of planar change by raising the wing tips. By varying twist distribution at the tips differently for each wing, a change in drag is created across the wing body, resulting in roll or yaw control. If the morphing changes at the tip are the same for each wing, such as along the trailing edge, there is a change in longitude similar to the effects of ailerons on a conventional wing.

Davidson *et al* (2003) investigated the flight dynamics of the HECS wing configuration and examined morphing at wing tip as well. The paper developed a nonlinear dynamic vehicle simulation and provided an assessment of stability and control for morphing maneuvers. The vehicle had a continuous morphing panel along the trailing edge of the wing for pitch and roll control along with a continuous wing tip used for roll and yaw control. The outer 30% of the half-span was the morphing region of the tip which could lift to provide roll control by increasing the projected area of the wing. The work discovered improvements in lift to drag, but unstable lateral-directional dynamics. A control system was designed to help stabilize the vehicle.

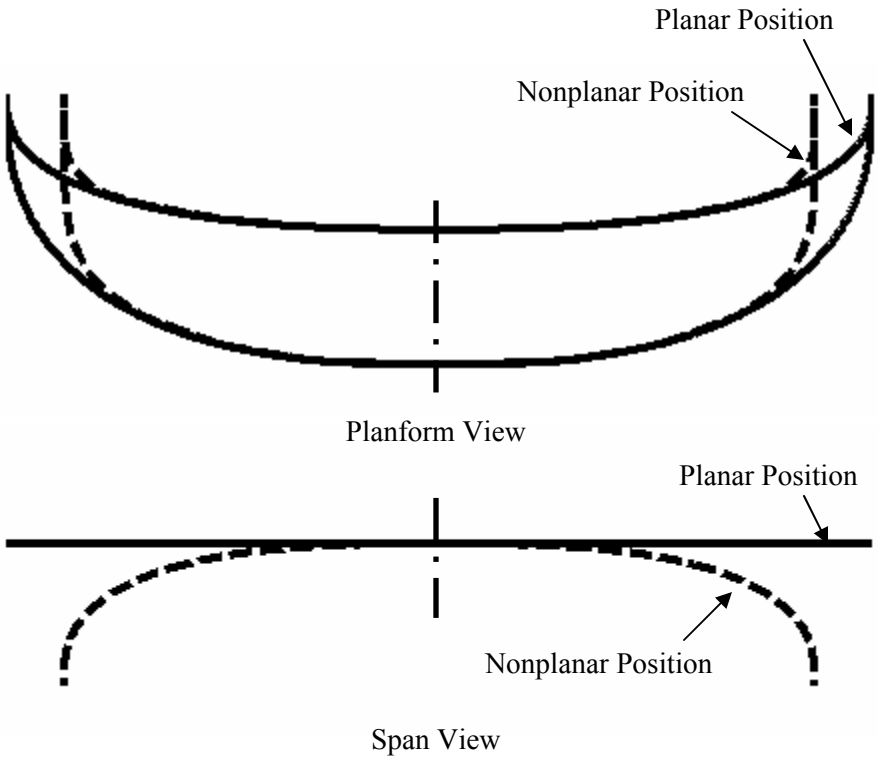

Figure 1.2: An illustration of final nonplanar and planar positions of the morphing HECS wing.

A kinematic mechanism was devised in order to carry out the goal of morphing the HECS wing. This design gave the ability to change the shape of the wing from its nonplanar to planar position, variable dihedral. If the mechanism were contained and actuated at the tip of the wing, planar motion along the tip of the wing would be possible. An aerodynamic study of the HECS wing at varying dihedral positions was also performed.

Development of a Kinematic Mechanism for Morphing

A kinematic mechanism was developed that achieves variable dihedral morphing of the HECS wing from a nonplanar to a planar position. The single-degree-of-freedom mechanism used a repeating quaternary-binary link arrangement in order to translate motion from one wing segment to the next. The quaternary links provided the main structure of the mechanism, while the two binary links actuated the quaternary links. This repeated quaternary-binary link configuration enabled motion to be translated from one segment to the next. A diagram of the quaternary-binary cross linked mechanism (QBCLM) is shown in Figure 1.3. The first link served as input to the mechanism through the binary links. Rotation of the quaternary link caused the following sections to rotate a prescribed amount. In order to produce the desired motion, the

dimensions of the linkage were determined through kinematic synthesis (Whittier, 2002 and Stubbs, 2003).

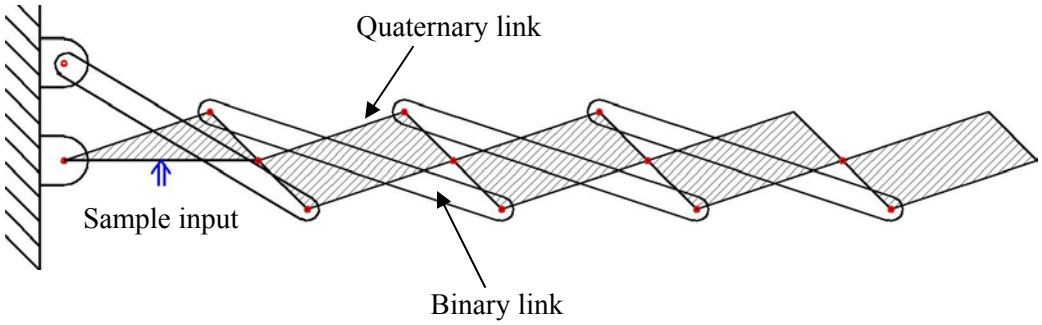

Figure 1.3: A diagram of the QCLM developed to morph the HECS wing.

The quaternary links form the main structure of the mechanism and hold the airfoil rib sections. The mechanism approximated the nonplanar shape in a linear piece-wise manner according to the number of quaternary links. The span of each of the quaternary links was defined by the distance between rib locations. Figure 1.4 shows the proposed rib locations, noted with triangles, in their nonplanar and planar positions. With the rib locations provided, there are a total of 11 sections of the wing. The locations of the attachment points of the binary links at each end gave way to four design variables for each section. Design synthesis techniques were developed in order to find the attachment points and produce a mechanism which has the desired shape. The synthesis, body guidance and other kinematic results were performed by Stubbs (Stubbs, 2003).

Proof-of-concept models were built in order to test the design of the mechanism. Theses replications were made to approximate dimensions and were beneficial hands-on visual representations of the design. The first generation of the two models that were built is pictured in Figure 1.5. The figure illustrates the input of a linear drive screw which moved a face plate that actuated the mechanism. The front view, picture at the top, shows the mechanism in an intermediate position. The picture on the bottom gives a better look at the mechanism. The boards running horizontal served as the quaternary links, while the slender diagonal beams were the binary links.

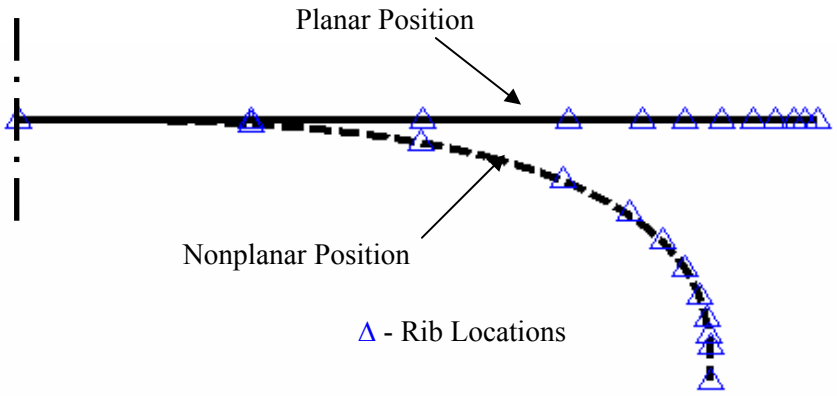

Figure 1.4: An illustration of the rib locations at nonplanar and planar positions.

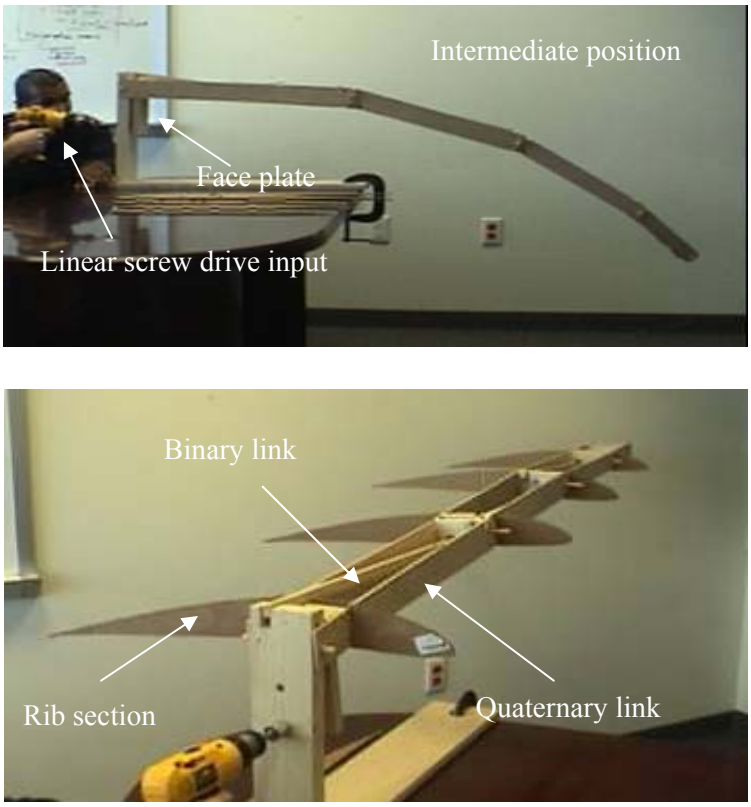

Figure 1.5: Pictures of the first generation 2-D concept model.

The second generation proof-of-concept model demonstrated the inclusion of sweep as well as an improved mechanism design. Pictures of the second generation model are shown in Figure 1.6. With the ends of the quaternary links cut at angles, this allowed the mechanism to sweep back. The binary links were replaced with threaded rod, and the first link was made

adjustable with a turnbuckle design. The turnbuckle allowed for an easy way to for adjust the length of the member. With the other design, the binary link had to be removed to adjust the length. The turnbuckle provided a way to adjust the length without having to remove parts. Metal brackets were also used to hold the rod ends which served as the revolute joints. This model showed the addition of sweep and also provided an improved mechanism design.

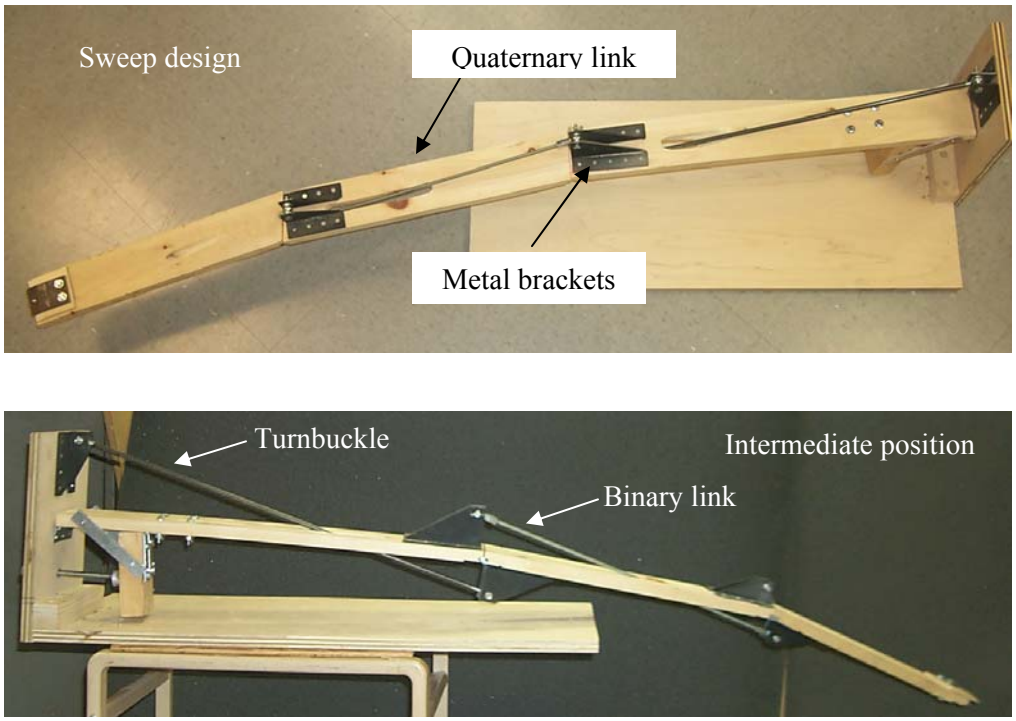

Figure 1.6: Pictures of the second generation concept model.

Aerodynamic Analysis of the HECS Wing

An aerodynamic analysis of the HECS wing configuration at various morphed positions was performed by Johnston. This study was based on a linear theory, nonplanar vortex lattice method. Aerodynamic spanwise load distributions for minimum drag were obtained while constraining the lift and pitching-moment coefficients and wing-root bending moment. Load distributions for the fully nonplanar, fully planar and half way between the two were predicted. These loads were to be used for an analytical structural study of the mechanism.

1.4 Thesis Overview

This thesis presents a structural analysis of the designed kinematic mechanism using Johnston's predicted aerodynamic loads of the HECS wing. All of the structural studies are linear static analyses. Chapter 2 includes the model developed for the 2-D analysis of the mechanism. The design approach and finite element model are detailed. Chapter 3 investigates nodal displacements and member forces and stresses under gravity loads and both aerodynamic and gravity loads. The study also provides an investigation of buckling in the two force binary link members as well. For gravity affects, it is shown that by using different material, the maximum deflection at the wing tip can be decreased while not approaching the critical loading of the elements. When both gravity and aerodynamic loads are tested, it is shown that the maximum stress exists in the binary link of the first section, as expected. The force does not cause the link to buckle though. A suggested redesign using lighter, but still structurally sound material is verified. Chapter 4 proposes modeling in 3-D space in order to examine the relative strength of the structure against twisting or torsion. A finite element model of the mechanism and rib structures are created. The results lead to some design suggestions for the mechanism.

Chapter 2

Two-Dimensional Structural Analysis Technique and Model

2.1 Analysis Technique and Structural Design

A two-dimensional structural design and analysis of the kinematic mechanism developed to morph the HECS wing is performed in order to evaluate the nodal displacement, and force, stress and buckling within the members. There are two analysis categories that are investigated which focus on the design of the binary and quaternary links. One category investigates the effects of only the gravitational forces (body forces) of the structure. The goal of this analysis is to reduce the maximum displacement of the structure through changes in the materials of the links. The strength-to-weight ratios of the materials and how they affect the displacement is the determining factor of the body force analysis. The other type of analysis includes the gravitational and predicted aerodynamic loads (surface forces). With the addition of the lifting loads, the binary links are examined according to a buckling margin of safety. Once it is determined that buckling is not an issue, a redesign of the quaternary links is explored. The factors of safety of the bending stresses of the quaternary links are used to compare the designs. The influence of these design changes on the overall displacement of the structure is another decisive factor.

Successive Analysis Approach

The method of design and analysis is a successive approach detailed by Rivello (1969) in *Theory and Analysis of Flight Structures*:

1. The determination of the critical combination of applied loads and temperatures to which the structure is subjected.
2. The layout of the design in which the arrangement, size, and materials of the component parts of the structure are tentatively decided upon.
3. The determination of the actual stresses and deformations in the structure due to the applied loads and temperatures.
4. The determination of the allowable stresses or deformations of the structure.
5. The comparison of Steps 3 and 4 to determine whether the design of Step 2 is adequate and efficient. If the design is either inadequate or overdesigned (and therefore inefficient), Steps 2 to 5 must be repeated until a satisfactory design is obtained.

This method can be applied to both the gravitational forces and the aerodynamic load and gravitational forces categories. The applied loads of Step 1 include the gravitational forces of the mechanism and the predicted aerodynamic loads. Whether it is just the gravitational forces or both the gravitational and aerodynamic forces depends on which analysis category is being performed. The layout of the structure is described later in this section and covers the arrangement of the structure mentioned in Step 2. The position of the mechanism is evaluated for three different cases. The positioning of the links and joints are not changed within the analysis, because of the nature of the design synthesis performed on the mechanism. By changing the lengths of members or moving the links or joints, the desired motion for morphing the wing may no longer be achievable. However, a redesign of the tentative cross section and material of the components is allowable and may be necessary if the design is inadequate as mentioned in Step 5. The determination of the stresses and deformation of the structure in Step 3 is performed with ANSYS models of the mechanism. These consist of static, linear elastic, isotropic models that evaluate the mechanism as a structure at three different positions. More of the ANSYS model is discussed in the next section, Section 2.2. The determination of allowable stresses of the structure depends upon the size and material of the components. These calculations are covered in Chapter 3, which also tells of Step 5, in which comparisons of the actual and allowable stresses dictate a redesign of the structure. Strength-to-weight ratio, margin-of-safety, and factor of safety criteria are used in order to decide whether or not a redesign is necessary.

Design and Layout of the Structure

As for the design and layout of Step 2, a half-span of the wing is modeled for the analysis. Since the wings are symmetrical, using a half-span model saves computation time and still produces reliable results. The mechanism is analyzed in three different positions: fully deflected, half deflected and flat. The fully deflected case replicates the original nonplanar HECS shape. Figure 2.1 shows a plot of the mechanism in the fully deflected case, that of the standard HECS wing. An input angle on the first link of -1.30 degrees is required in order to achieve this shape. The half deflected case is an arbitrarily picked position half way between the fully deflected and flat case. A plot of the mechanism in the half deflected position is shown in Figure 2.2. An input angle of -0.650 degrees is required to achieve the half deflected case. For the flat case, an input angle of zero is required, and this represents the fully planar position of a morphed HECS wing. The mechanism is plotted in Figure 2.3 for the flat case.

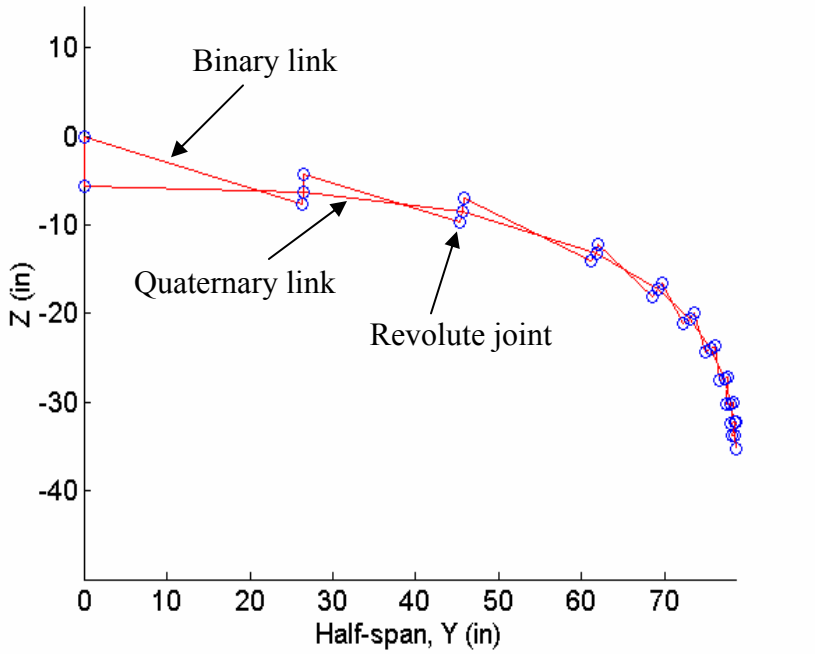

Figure 2.1: Plot of the mechanism in its fully deflected position.

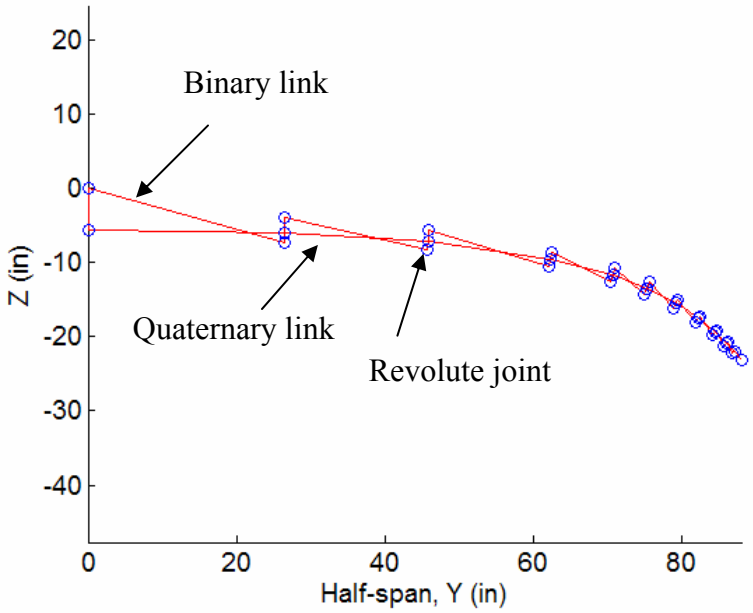

Figure 2.2: Plot of the mechanism in its half deflected position.

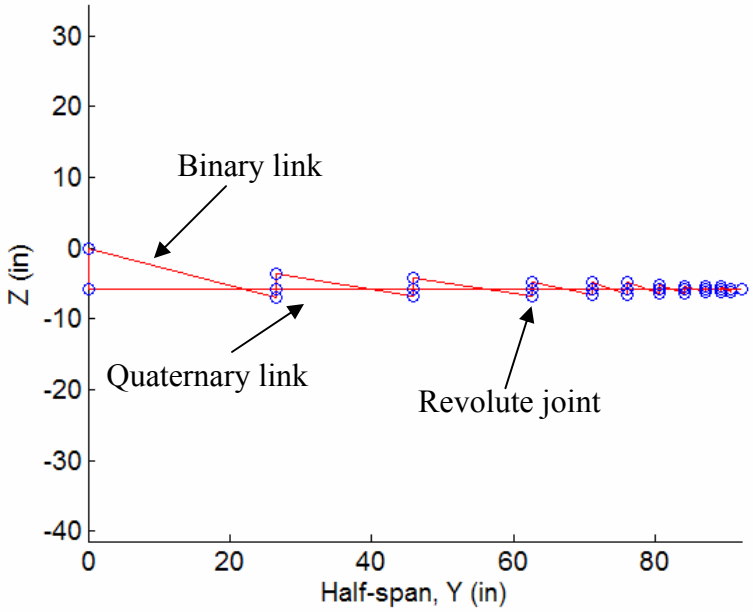

Figure 2.3: Plot of the mechanism in its flat position.

According to the aerodynamic analysis, the configuration in which the wing experiences the most extreme loading conditions is the flat case. This is because of the larger moment produced on the wing since it has the longest span of the three cases. Therefore, the primary design analysis is performed on the flat position of the wing. However, to ensure completeness of the design, once a satisfactory design has been established for the flat case, the half and fully deflected positions are investigated. These analyses use the cross section and material characteristics of the final design determined from the flat case, but are examined as a failure check of the structural design for different morphed positions. Even though the load distributions for the half and fully deflected cases are less than that of the flat, a redesign at those positions may be necessary in order to be confident in the final satisfactory design.

2.2 Two-Dimensional ANSYS Model Development

ANSYS finite element model representations of the mechanism are developed in order to determine the stresses and deformation of the structure. When modeling in ANSYS, the second generation proof of concept model developed in Chapter 1, Figure 1.7, is taken into design consideration for the tentative cross section and material of the components. The elements and boundary conditions of each of the three positions of the mechanism do not change within the analyses. The binary links of the mechanism are modeled as LINK1 elements, 2-D spar truss elements. There are two translational degrees-of-freedom per node with these elements. This is a good representation of the binary links of the mechanism, because they act as two force members that receive axial tension and compression along one axis with no bending. The quaternary links are modeled with BEAM3 elements. These elements have uniaxial tension, compression and bending with three degrees-of-freedom, two translational and a rotational, per node which are an accurate representation of the concept model. The metal brackets of Figure 1.7 are also modeled as BEAM3 elements. These brackets experience tension and compression as well as bending moments caused by the binary links and the applied forces making the beam elements a good representation. This makes for three different groups or types of elements.

Three real constant sets are also defined in ANSYS, one for each of the three element types. These constants define parameters such as cross sectional area, area moment of inertia, and beam height. For the first tentative design, the binary link members are set with a circular cross section and the area is defined by the radius. For the quaternary beam links, a rectangular

cross section is chosen with the area and area moment of inertia depending on the height and width of the cross section. The same is used for describing the constants of the brackets; however, the orientation of the cross section differs from that of the quaternary links and therefore differs in height and width. A shear deflection constant of 1.2 is used for both of these rectangular cross section beams.

Like the real constant sets, three material models are created, one for each of the three element types. Each model defines a material density as well as linear, elastic isotropic values of modulus of elasticity, and Poisson's ratio. As with the real constants sets, the first tentative designs are modeled after the second generation model. The binary and bracket links are given values of a plain carbon and low alloy steel. While, the quaternary links are modeled with isotropic soft wood properties.

With the elements, real constants, cross sections and material models in ANSYS, the actual geometry of the structure is entered. Using the defined location of the links and revolute joints as shown in the plots of the mechanism, Figures 2.1-2.3, log files are written in MATLAB which define keypoints at the revolute joint locations. These keypoints are converted to nodes and used to create the actual elements of the ANSYS models. These elements are made with attributes according to the element type. For example, when the binary links are created, it is made certain that they use the corresponding LINK1 elements, real constant sets, circular cross sections, and material models. The same logic applies to the quaternary and bracket links. Note that the rigid ground link of the structure, the vertical link at the root of the half-span, is given beam element characteristics.

Once the boundary conditions and loads are applied, the two-dimensional ANSYS model of the mechanism can be solved for the stresses and deformations of the structure. The boundary conditions are the same throughout all of the analyses. The displacements of the two nodes of the ground link are held with a prescribed value of zero for its degrees-of-freedom. This provides the structure with a rigid ground support. As mentioned earlier, there are two types of applied loads analyzed: gravitational forces, which are body forces, and aerodynamic loads, which act as surface forces. The gravitational forces are simulated through the ACEL command of ANSYS. Through that command, the densities of the materials are taken into account to create defined gravity loads. Figure 2.4 shows the fully deflected case modeled with boundary conditions and a defined acceleration in the positive y direction for gravity. Essentially, the structure is being

accelerated in a direction opposite to gravity. The surface forces in the form of the predicted aerodynamic loads are applied at the nodes where the quaternary links meet in each chain link of the structure. An illustration of a fully deflected model which exhibits both gravitational and aerodynamic loads is shown if Figure 2.5. The structure experiences a lifting force as well as a force to the side in the direction of the tip of the wing. These forces in both directions are applied to the model, although it may be difficult to distinguish in the figure because of the comparatively low amplitude of the side loads and loads towards the tip. The flat case does not experience any side force however.

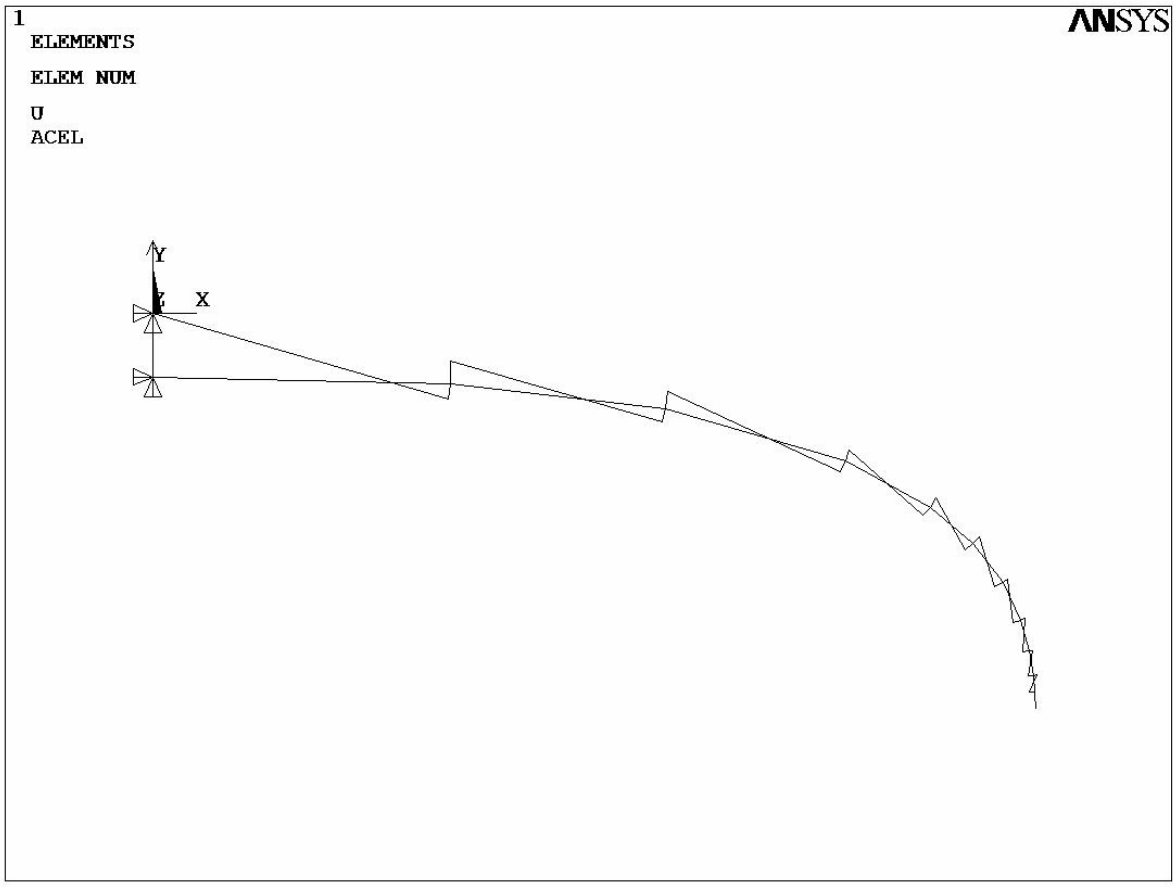

Figure 2.4: Illustration of the two-dimensional structure modeled in ANSYS with defined gravitational forces for the fully deflected case.

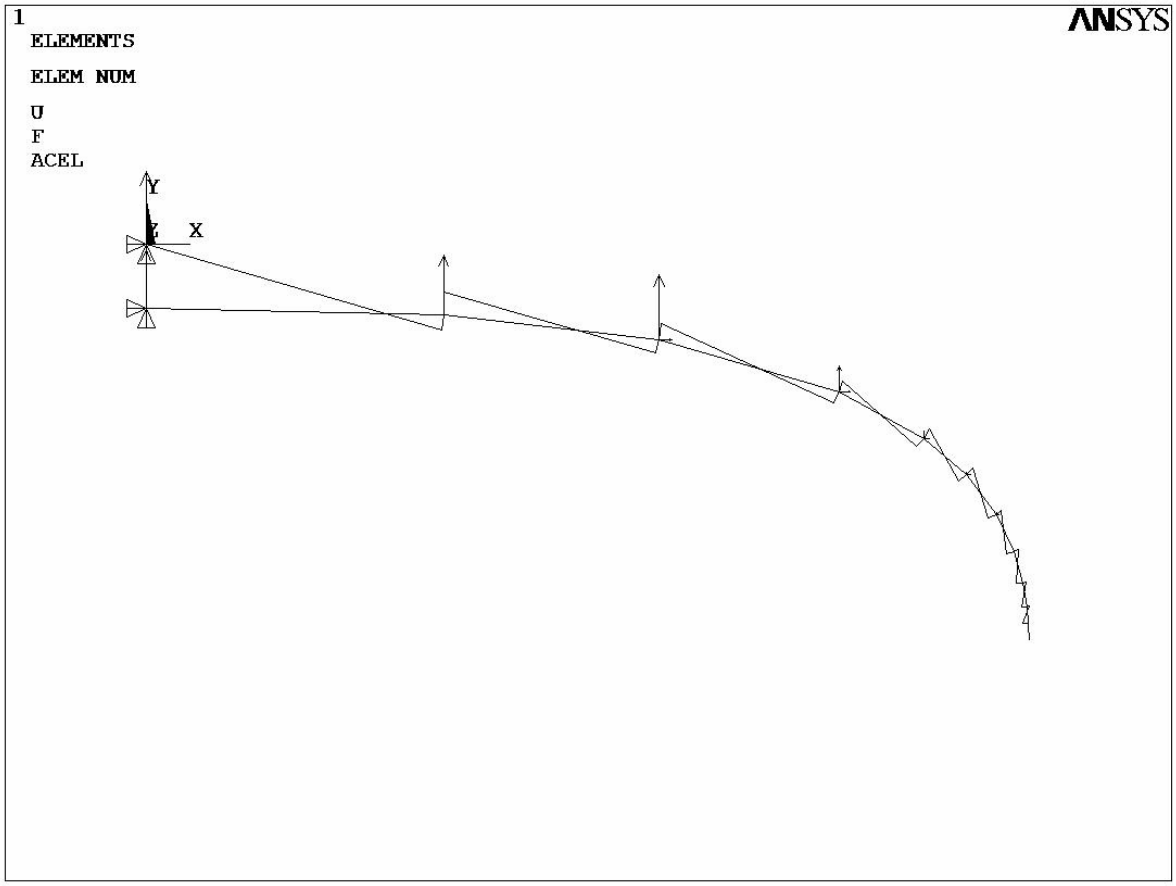

Figure 2.5: Illustration of the two-dimensional structure modeled in ANSYS with applied aerodynamic and defined gravitational forces for the fully deflected case.

Application of Predicted Aerodynamic Loads

Predicted aerodynamic load distributions are found according to MATLAB code produced by Johnston (Wiggins *et al*, 2004). The loads simulate a 2g pull up maneuver. This case is chosen because the loads now serve as ultimate load conditions the mechanism experiences during flight. These distributions are found for the flat and fully deflected cases of the HECS wing. Concentrated forces are used to represent the applied loads through the revolute joint nodes at the quaternary links. Therefore, numerical integration of an area surrounding the rib locations is performed. It is ensured that each rib location is the midpoint of the boundaries of its section. Once the numerical integration is performed on a section, the result is a concentrated load at the specified rib location, which corresponds to the revolute joints of the mechanism. Figure 2.6 shows the lifting force load distribution for the flat case. Figures 2.7 and 2.8 show the

lift force and side force of the wing, respectively, at its fully deflected position. The points marked with an *x* on the graphs represent the rib locations. There is no side force for the flat position. A comparison of the lifting force of the graphs also shows how the longer span of the flat case results in a larger bending moment justifying using this case as the primary structural concern. With the concentrated loads for the flat and fully deflected cases, an average of these values is taken in order to determine forces for the half deflected case. Since this is a linear analysis, this assumption is valid. Tables 2.1 – 3 show the concentrated forces that are applied to the nodes to represent the aerodynamic loads on the mechanism.

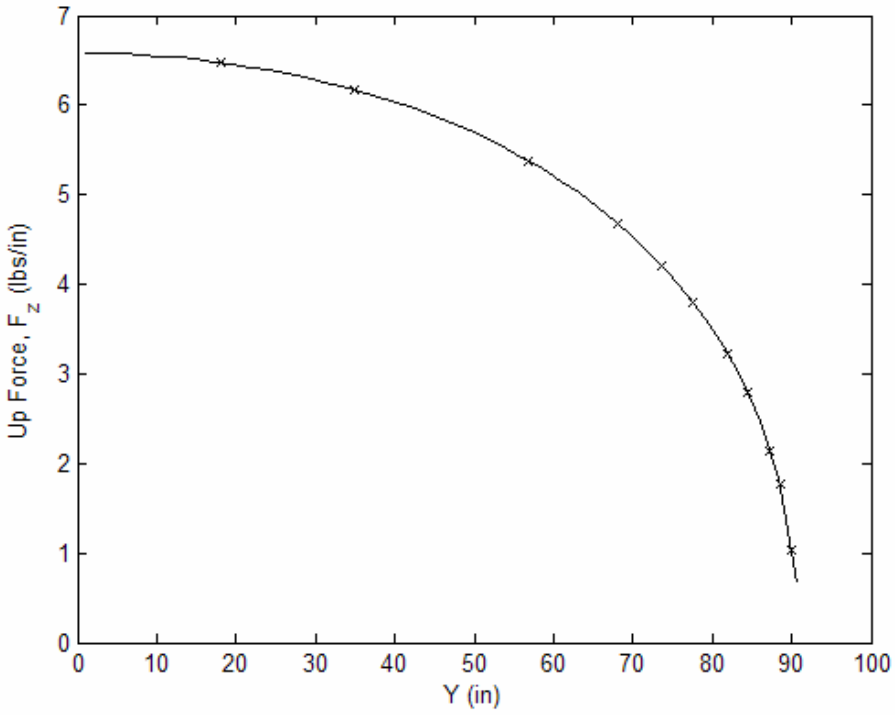

Figure 2.6: Plot of the lifting force distribution across the morphed HECS wing in its flat position.

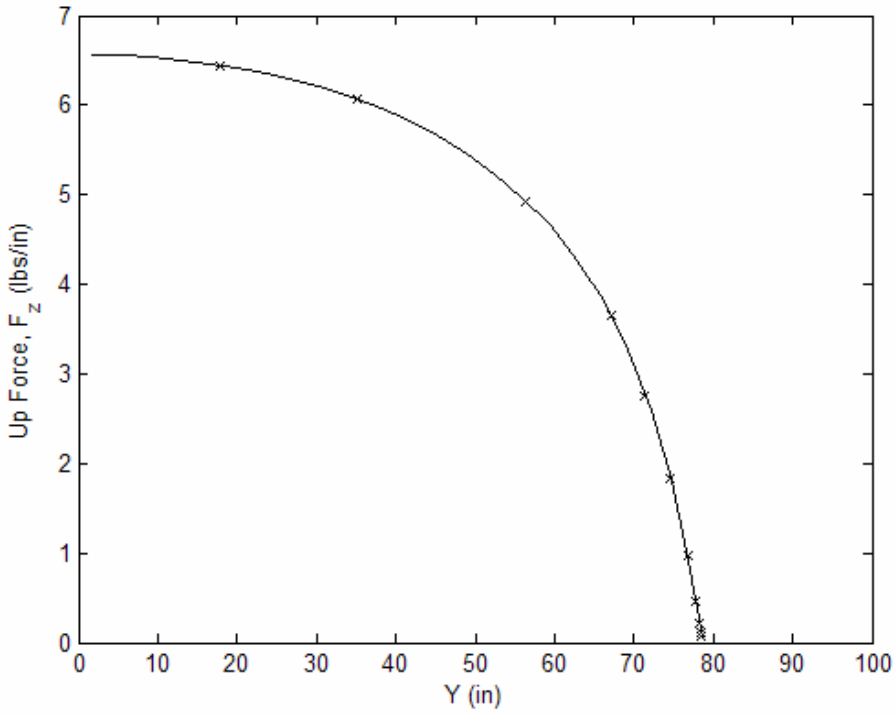

Figure 2.7: Plot of the lifting force distribution across the morphed HECS wing in its fully deflected position.

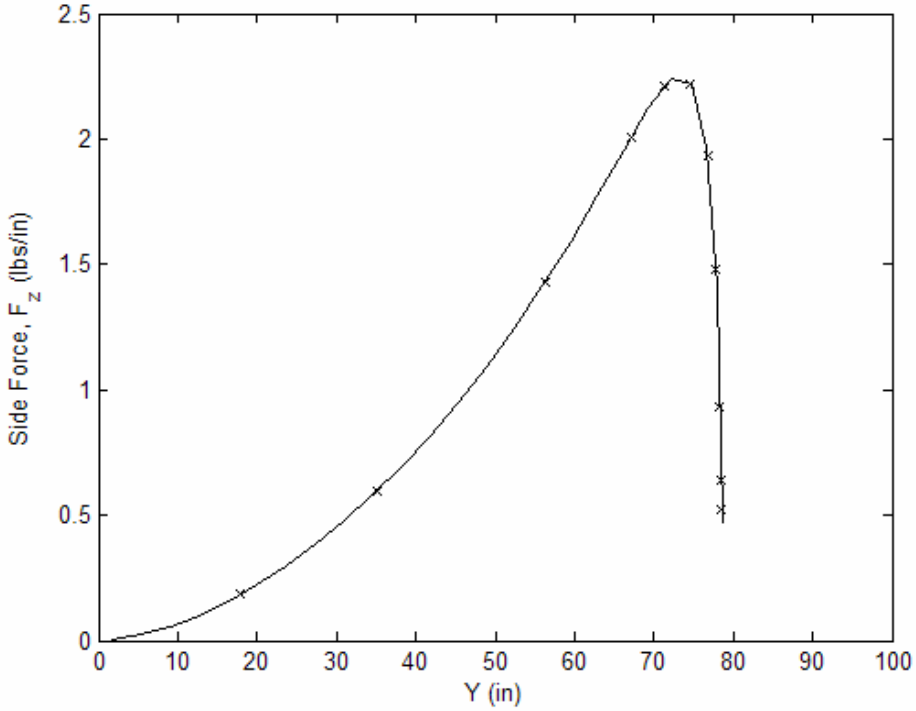

Figure 2.8: Plot of the side load distribution across the morphed HECS wing in its flat position.

Table 2.1: Summary of the applied nodal aerodynamic loads for the flat case.

Up Force (lbf)	Side Force (lbf)
110.9	0
105.5	0
126.7	0
56.56	0
24.00	0
15.97	0
15.27	0
7.626	0
6.709	0
2.483	0
2.031	0

Table 2.2: Summary of the applied nodal aerodynamic loads for the half deflected case.

Up Force (lbf)	Side Force (lbf)
107.9	0.7667
106.2	3.341
122.0	10.81
51.29	9.226
19.42	4.553
11.67	3.558
9.119	2.206
4.188	0.8919
3.439	0.3033
1.257	0.0781
1.019	0.0234

Table 2.3: Summary of the applied nodal aerodynamic loads for the fully deflected case.

Up Force (lbf)	Side Force (lbf)
104.9	1.533
106.9	6.681
117.3	21.63
46.01	18.45
13.84	9.107
7.366	7.116
2.968	4.411
0.7492	1.784
0.1694	0.6066
0.0314	0.1562
0.0069	0.0467

2.3 Chapter Summary

A description of the two-dimensional structural analysis technique and details of the design and ANSYS model are presented in this chapter. A successive method, which is an iterative type approach, is used to examine the criteria of the analysis. Two analysis categories are performed during the tests, one with gravitational loads and the other with gravitational and aerodynamic loads. The design layout of the structure is also discussed along with how the ANSYS model is developed to represent the details of the structure. Concentrated loads are found from the predicted aerodynamic load distributions in order to have applied forces for the nodes of the model. In Chapter 2, an analysis method, accurate structural design and model, and applied loads are specified. The following chapter develops a 3-D model along with suggested redesigns of the structure.

Chapter 3

Two-Dimensional Structural Analysis and Results

3.1 Introduction to the Two-Dimensional Structural Study

Tests are performed on the flat position of the morphed HECS wing since this case produces the most extreme bending moment on the root of the wing. Two basic structural analyses are carried out on the mechanism in this flat position. One analysis investigates the effects of the weight of the structure by using a gravitational study. The other analysis uses the predicted aerodynamic loads as well as the structural weight of the mechanism. Both of the analyses follow a successive or iterative type approach covered in Section 2.1. Also note that the binary links are labeled from B1 to B10 and the quaternary links from Q1 to Q10 from root to tip, respectively, as shown in Figure 3.1. Tests are also performed on the fully and half deflected positions. These tests use the final design that is achieved from the successive analysis approach of the flat case. The fully and half deflected cases are used as more of an investigation to check for the displacement under gravitational loads or for buckling or bending stress failure. Analysis and test results for all three cases are covered along with some verification calculations of the results of a simplified ANSYS model.

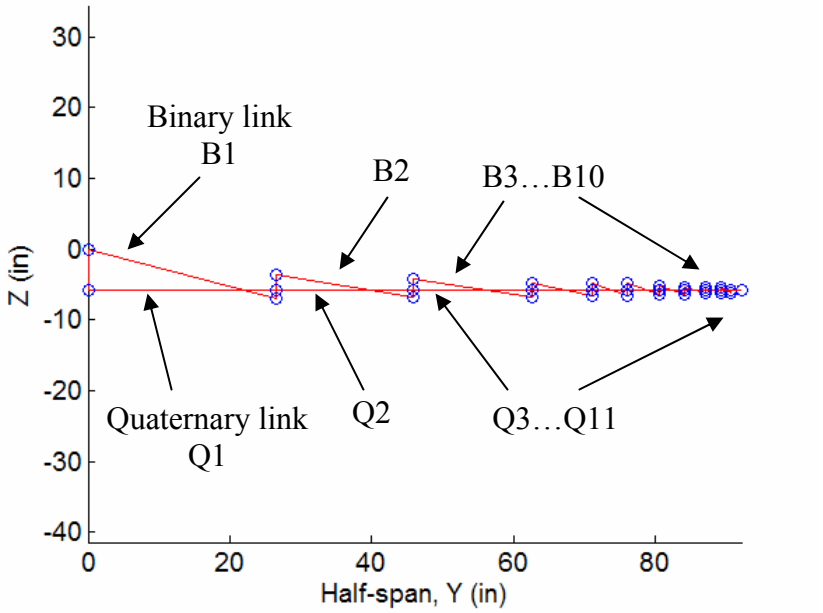

Figure 3.1: A diagram of the labeling for the binary and quaternary links of the structure.

3.2 Gravitational Analysis of the Flat Case

Test runs are performed to investigate the effects of gravity on the structure in its flat position. Materials, real constants, and cross sections are set in the ANSYS model for the binary, quaternary, bracket, and ground links. ANSYS is used to determine the stress in the members and the deflection of the structure. Calculations are performed to determine the strength-to-weight ratio factor used to establish if the structure should be redesigned according to its deflection. In order to find the strength-to-weight ratio, the ultimate tensile strength of the material is divided by its weight density.

For the initial design and first test run, materials of the second generation model are used as a starting point. The binary links, LINK1 truss elements, are assigned with a plain carbon and low alloy steel with a Young's modulus of 3E7 psi, an ultimate tensile strength of 1.15E5 psi, and a weight density of 7.33E-4 lbf-s^2/in^4. The binary links are also given a circular cross section with a radius 0.125 in. The quaternary links, BEAM3 elements, are modeled with soft wood properties. Its material properties consist of a Young's modulus of 0.8 psi, an ultimate tensile

strength of 230 psi, and a weight density of 2.85E-5 lbf-s^2/in^4. A rectangular cross section is used for the quaternary links with a width, *b*, of 3.5 in. and height, *h*, of 0.75 in. The bracket links, also BEAM3 elements, are modeled with the same plain carbon material as the binary links. They are given a rectangular cross section with $b = 0.125$ in. and $h = 0.875$ in. The ground link, BEAM3 element, is given the same soft wood material properties and rectangular cross section as the quaternary links.

When the model is solved to investigate gravity effects for the first run, a maximum displacement of 2.12 in. occurs at the tip of the structure. The materials and corresponding strength-to-weight factors of the links are shown in Table 3.1. The axial stress experienced in the binary links is shown in Table 3.2. The maximum tensile stress occurs in the first link as expected. This value of 952.1 psi does not approach the ultimate tensile strength of 1.15E5 psi of the plain carbon and low alloy steel material in which it is modeled with. This shows that the binary links are not approaching failure in tension from the weight of the structure.

In order to decrease the maximum displacement due to gravity, more tests are run using this model. Only an investigation of different materials is used for the gravitational study. The cross sectional areas of the links remain the same. The general trend follows that as the strength-to-weight ratio increases for the chosen material, the resulting maximum displacement of the structure decreases. A design choice of Aluminum Alloy 7075 T651 is made for the binary, quaternary, and ground links. The bracket uses the same plain carbon and low alloy steel material of the first test run. The maximum stress occurs in the first binary link member as shown in Table 3.3. The design with these materials leads to the aerodynamic and gravitational loads analysis. The maximum displacement of the structure is reduced from 2.12 in. of the initial design to 1.22 in. for the completed gravitational analysis design. Figure 3.2 shows an illustration of the deflection of the structure where the maximum displacement occurs at the tip.

Table 3.1: Summary of the links, materials, and strength-to-weight factors for the first run.

Link	Material	Strength-to-weight (in^2/s^2)
Binary	Plain carbon and low alloy steel	1.57E8
Quaternary	Soft wood	8.07E6
Ground	Soft wood	8.07E6
Bracket	Plain carbon and low alloy steel	1.57E8

Table 3.2: Axial stress of the binary links in tension for the first run.

Binary Link	Member Length (in)	Axial Stress (psi)
B1	27.41	952.1
B2	19.60	820.8
B3	16.89	399.0
B4	8.800	76.45
B5	5.291	42.56
B6	4.691	31.25
B7	3.891	6.589
B8	3.009	0.2864
B9	2.287	0.2462
B10	1.649	0.5672

Table 3.3: Axial stress of the binary links in tension for the third run. The ultimate tensile strength of the Aluminum Alloy material is 8.27E4 psi.

Binary Link	Member Length (in)	Axial Stress (psi)
B1	27.41	3997.7
B2	19.60	1149.7
B3	16.89	434.18
B4	8.800	54.30
B5	5.291	26.48
B6	4.691	18.24
B7	3.891	3.057
B8	3.009	-1.42E-2
B9	2.287	9.26E-3
B10	1.649	0.2526

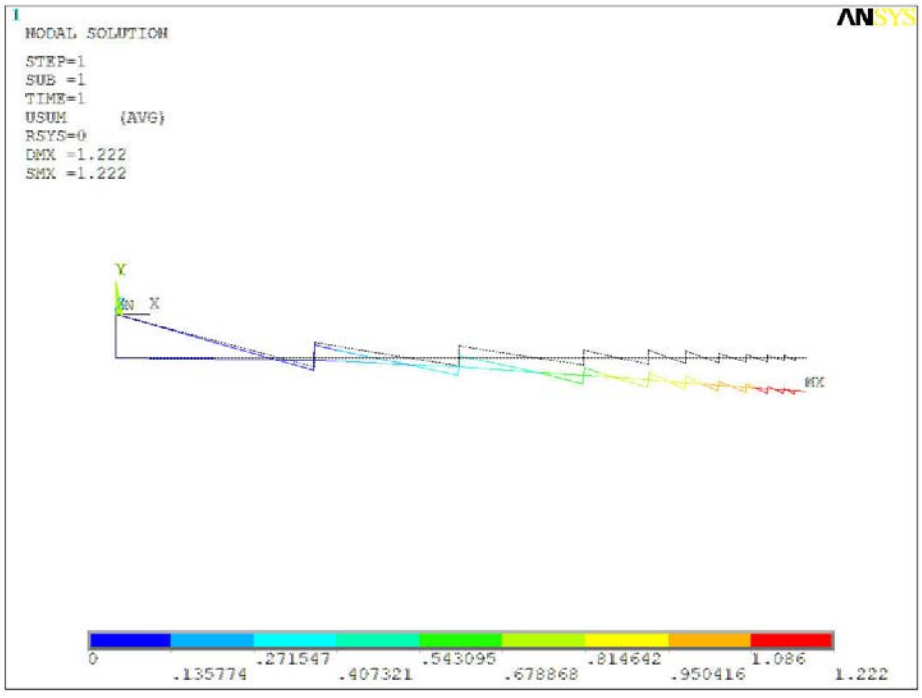

Figure 3.2: ANSYS plot of nodal displacement results from completed design of the gravitational analysis of the flat case.

3.3 Aerodynamic and Gravitational Load Analysis of the Flat Case

There are actually two phases of the aerodynamic and gravitational load analysis. One phase focuses on reducing the buckling margin of safety in the binary links. The other phase attempts to reduce the maximum bending stress of the quaternary links. As in the gravitational analysis, materials, real constants, and cross sections are set in the ANSYS model for the binary, quaternary, bracket, and ground links. ANSYS is used to determine the axial stress, bending moment in the members and the deflection of the structure. The results and designs of the buckling and bending moment phases are covered.

Buckling Analysis Phase

For the first phase, the predicted aerodynamic loads are applied to the structure and buckling is investigated starting from the design of the last test run of the gravitational analysis. There is a potential for buckling with the two-force binary members because of the applied load. As discovered, the way in which the members are analyzed for buckling depends on the length of the link. The binary links are identified as B1 through B10 from root to tip the same as in the gravitational analysis.

For the analysis, the limit loads are the largest anticipated loads the structure will experience during its lifetime. It is impractical to set the loads at a level in which the structure will never fail, because the design will be inefficient from a weight standpoint. Therefore, the limit loads are set at a level which results in an acceptable low level of failure. A factor of safety of 1.5 is used for inhabited aircraft. The ultimate load is defined as the limit load multiplied by the factor of safety (Rivello, 1969). Aircraft components are designed to survive the ultimate load conditions (Curtis, 1997).

A buckling margin of safety factor is used to examine the design effectiveness of each test run. The margin of safety is calculated by dividing the critical stress by the limit stress and subtracting one. The limit stress is found by using the member stress determined through the ANSYS model as an ultimate stress. This ultimate stress is divided by a safety factor of 1.5 in order to have the limit stress. The critical stress is found by dividing the critical force by the cross sectional area of the binary link. The formula for the critical force is,

$$P_{cr} = \frac{\pi^2 EI}{L^2} \tag{3.1}$$

where E is the Young's modulus, I is the area moment of inertia, and L is the member length. The goal of this phase of test runs is to decrease the margin of safety in the binary links. There must be a positive margin of safety, but lightweight structures are designed so that the margin is as small as possible (Curtis, 1997).

For the initial design and first test run, it is found that the binary link with the highest axial stress is the first member as expected. It also has the lowest buckling margin of safety of 12.5. This first design has a constant radius for each binary link and a maximum displacement of 15.75 in. at the tip. The remaining test runs investigate using varying radii for the members. This provides an opportunity to decrease the margin of safety for not just the first link, but the others as well, making the structure more lightweight. An examination of the slenderness ratios of the final two links shows that they are short columns and can not be examined for buckling like the other long links. A short column has a slenderness ratio less than 10. The slenderness ratio is defined as,

$$S_r = \frac{l}{k} \tag{3.2}$$

where l is the length of the member and k is the radius of gyration. The equation for the radius of gyration is,

$$k = \sqrt{\frac{I}{A}} \tag{3.3}$$

where I is the area moment of inertia of the cross section and A is the cross sectional area. The final two binary links have slenderness ratios of 9.15 and 6.60, respectively. A table of the slenderness ratio for each binary link can be found in Appendix A. For these links, the yield strength of the material versus the axial stress is used as the determining factor (Norton, 1998).

For the final design of the buckling test phase, the radius of the first link is increased from 0.125 in. for the initial design to 0.3 in. in the final design. In turn, this decreased the buckling margin of safety from 12.5 to 0.010 as compared to the first test run. The results of link B1 were influenced by the redesign of the other binary links as well. For binary links B2 through B8, the radius of B2 is the only one that can be changed to have a significant decrease in the margin of safety without having to make the radius considerably small. In order to avoid trivial results and to make parts easier to manufacture, the radius of links B3 through B10 are kept constant at 0.002 in. It is found that the member with the major influence on the displacement of the structure is B1. The radius of member B2 is made smaller since its margin of safety can be decreased to a factor of 0.125 compared to 29.5 for the first run. The axial stresses of the short column members B9 and B10 result in 0.222 and 1.1086 psi in tension, respectively. These stresses do not approach the yield strength of 73,200 psi of the material, Aluminum Alloy 7075 T651. The final design of those links will not fail under buckling. The final design of the buckling phase has a deflection of 14.195 in. compared to 15.75 in. from the design of the first test run. The final design proves to stiffen the structure as well. Figure 3.3 shows the deflection of the design in ANSYS.

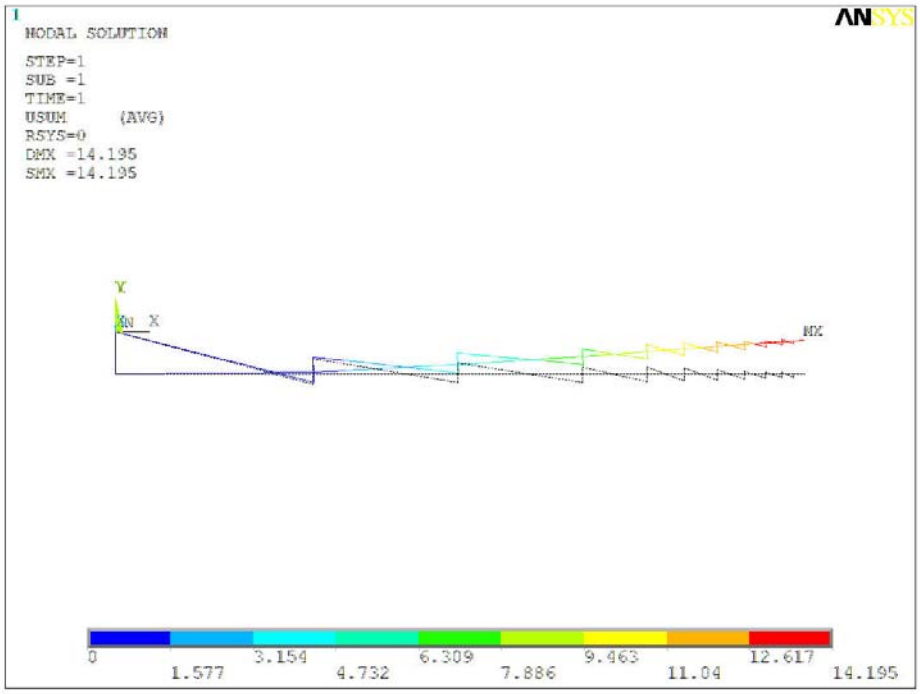

Figure 3.3: ANSYS plot of nodal displacement results from completed design of the buckling phase of the aerodynamic and gravitational load analysis of the flat case.

Bending Stress Analysis Phase

Starting from the design of the buckling phase, a reduction of the maximum bending stress of the quaternary links is examined. Modeled as beams, the bending stress occurs on the underneath side as the resulting applied load bends the beam upward. This is the side which is put into tension by the bending of the beam. Throughout the analysis for the bending stress, the buckling of the binary links is still examined in order to determine how they react to the design of the beam sections. The quaternary links are labeled Q1 through Q11 as illustrated in Figure 3.1. There is one more quaternary link than binary link because of the final section at the tip of the wing which is modeled as a quaternary link.

A factor of safety criterion is used to evaluate the designs of each run in the bending stress phase. The factor of safety is found by dividing the yield strength of the material by the actual bending stress. The yield strength of Aluminum Alloy 7075 T651 is 73,200 psi. The actual bending stresses are found through the ANSYS solution. The solutions are chosen ANSYS element table results from the negative side of each beam element since the beam is in tension when bending upward. A factor of safety of 1.5 is usually the standard for inhabited aircraft. It is a lower factor of safety than that used by other civil or machine structures, but they require extensive analysis and tests (Rivello, 1969). This lower factor of safety also helps in the design of more lightweight structures needed for aircraft. The goal of the tests is to approach a factor of safety around 1.5 and to decrease the maximum displacement of the structure.

All cross sections of the quaternary links of the structure are modeled the same for the first test run. The height of the beam section h = 0.75 in and the width b = 3.5 in. The section which has the highest bending moment and stress is link Q1. It has a bending moment of 12,087 lb-in, an actual bending stress of 36,851 psi, and a calculated maximum bending stress of 36,836.6 psi. The first section also has the lowest factor of safety of about 1.99. Table 3.4 shows the actual bending stress and factor of safety for each quaternary beam link for the first test run. However, the maximum displacement with this design is 14.2 in.

Table 3.4: Bending stress of factor of safety for the beam elements with an initial test run of cross sectional height of 0.75 in. for each link.

Quaternary Link	Actual Bending Stress (psi)	Factor of Safety
Q1	36851.0	1.99
Q2	10033.0	7.30
Q3	3222.5	22.7
Q4	1421.2	51.5
Q5	728.68	100.4
Q6	313.95	233.2
Q7	124.97	585.7
Q8	37.695	1941.9
Q9	11.101	6594.0
Q10	1.9639	37272.8
Q11	-2.80E-10	2.6E14

A change in the cross sectional height is investigated in order to decrease the factors of safety of the members following the first section and to decrease the maximum displacement of the structure. It is chosen to investigate the use of different heights from root to tip of the structure. This serves as a way to reduce some of the weight of the structure towards the tip where the loads are not as high. When choosing heights for the sections, maximum heights of the links are determined. These heights are based on a designed "box" in which the structure can still fit within the structure of the wing. This "box" is found by first establishing the location of the maximum thickness of the airfoil. For the SD 7032 airfoil section, the maximum thickness location is 9.99% at 28.2% of the chord. A box shape is then extrapolated to marginal percentages that still allow the mechanism to lie within the chord. The importance of this "box" is that it gives a maximum height range to work in. Figure 3.4 shows an example airfoil section and the determined "box" which gives a maximum height envelope for the mechanism. Table 3.5 shows the maximum heights for each quaternary link of the structure.

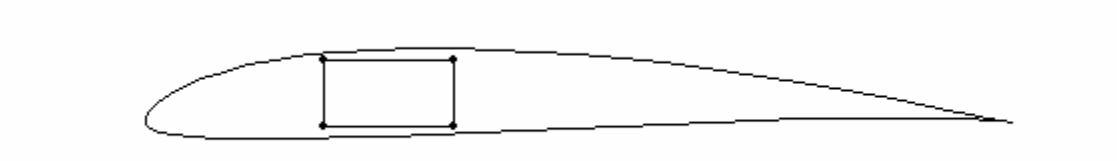

Figure 3.4: An illustration of the SD 7032 airfoil and the mechanism "box" extrapolated from the location of maximum thickness of the airfoil.

Table 3.5: Maximum heights of the quaternary link beam sections

Quaternary Link	Maximum Height (in)
Q1	2.177
Q2	2.136
Q3	2.010
Q4	1.783
Q5	1.600
Q6	1.454
Q7	1.296
Q8	1.126
Q9	0.954
Q10	0.775
Q11	0.598

The results of the test runs of the bending stress analysis show that the beam sections can be tailored by cross sectional height in order to reduce weight and bending stress. It is determined, much like the results of the buckling phase analysis, that the first member experiences the highest bending stress and has the lowest factor of safety. It also shows that in order to decrease the maximum displacement of the structure, the height of the first quaternary link has to be increased. By increasing this height, the factor of safety for the first link is also increased. For instance, for one of the test runs, a chosen height of 0.667 in. for the first link gives a factor of safety of 1.5. The maximum displacement of the structure is about 23.2 in. however. To allow for a decrease in the maximum displacement at the tip of the structure, a

higher factor of safety is allowed. Since the first link experiences the lowest factor of safety, it is the focus of designing based on the factor of safety.

A design which increases the heights of sections Q1 through Q8 and reduces the heights of sections Q9 through Q11 from the height of 0.75 in. used in the first test run is determined. This gives a lighter structure towards the tip, while decreasing the bending stress near the root. Table 3.6 shows the cross sectional heights and maximum bending stresses of the final design chosen for the bending stress phase. The lowest factor of safety of 9.37 occurs at the first quaternary link. This shows the structure will not fail from the bending stresses. A maximum displacement result of 2.2 in. at the tip of the structure also results from this design. The design can withstand the maximum bending stresses and a reduction in maximum displacement from the original design is found.

Table 3.6: Cross sectional height and maximum bending stress for each beam element for the final design chosen.

Quaternary Link	Cross Sectional Height (in)	Actual Bending Stress (psi)
Q1	1.50	7815.7
Q2	1.50	2284.7
Q3	1.50	784.53
Q4	1.25	505.85
Q5	1.25	263.88
Q6	1.25	116.83
Q7	1.00	75.484
Q8	1.00	24.254
Q9	0.50	29.931
Q10	0.50	5.9405
Q11	0.25	-1.63E-10

Compared to the original design, with the final design, the actual bending moment is reduced from 12,087 lb-in to 10,258 lb-in and the actual bending stress is reduced from 36,851 psi to 7,815.7 psi. This is achieved through the tailoring of sectional heights. As a consequence to the added weight of the structure, the buckling margins of safety of the first and second binary

links increase. At the initial test run, links B1 and B2 have a margin of safety of 0.09876 and 0.1245, respectively. The margin of safety for links B1 and B2 with this final design are 0.6946 and 6.877. These numbers are higher than the initial, but are reasonable compared to the increased structural support and factors of safety. A change in the factors of safety can also be achieved by not just changing the height of the cross sections, but by using different materials that have a different stiffness then the one used for this model. Also, the maximum displacement at the tip of the structure is decreased from 14.195 in. for the initial design to 2.02 in. for the final design of the bending stress phase. This decrease in deflection also legitimizes the slight increase in buckling margins of safety for the binary links. The ANSYS plot of the displacement of this final design is shown in Figure 3.5.

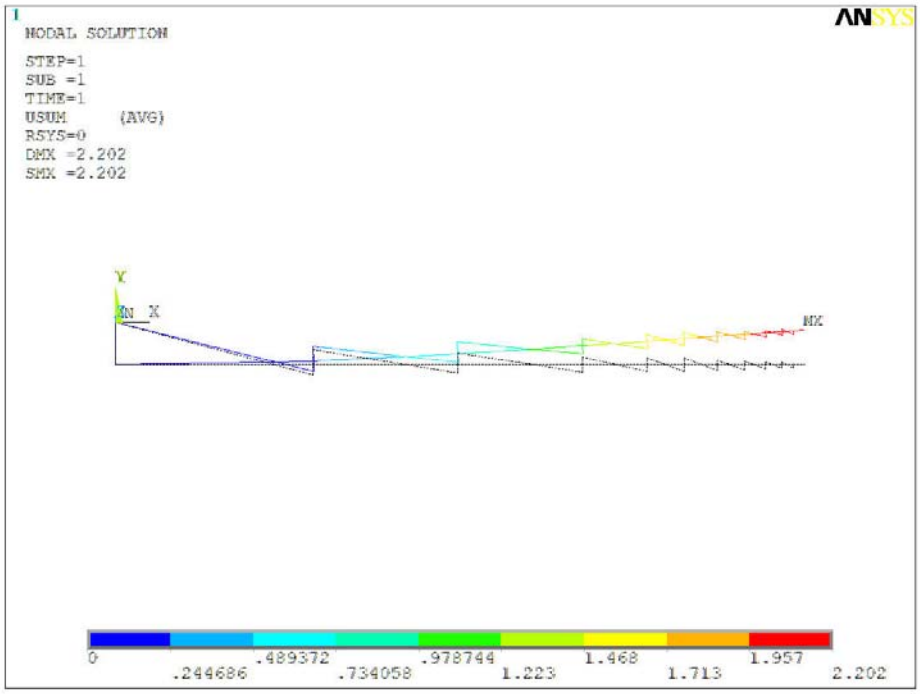

Figure 3.5: ANSYS plot of nodal displacement results from completed design of the bending stress phase of the aerodynamic and gravitational load analysis of the flat case.

A sanity check of the bending stresses produced by ANSYS is performed. The check of the bending stresses is found by dividing the maximum bending stresses by the actual bending stresses. The maximum bending stresses are found mathematically through,

$$\sigma_{max} = \frac{Mc}{I} \tag{3.4}$$

where M is the applied bending moment, c is the distance from the neutral axis to the top or bottom outer fiber of the beam, and I is the area moment of inertia of the beam cross section (Norton, 1998). The applied bending moment for each beam is found from the ANSYS model. If the stresses check, they should be close to a value of 1. A summary of the check of the bending stresses is shown in Table 3.7. It is shown that the design of each link is approximately equal to 1.0 and the final design checks.

Table 3.7: A summary of the sanity check of the maximum bending stresses for the final design.

Quaternary Link	Cross Sectional Height (in)	Actual Bending Stress (psi)	Check Value
Q1	1.50	7815.7	0.99999
Q2	1.50	2284.7	1.00000
Q3	1.50	784.53	1.00000
Q4	1.25	505.85	1.00001
Q5	1.25	263.88	0.99998
Q6	1.25	116.83	1.00004
Q7	1.00	75.484	0.99999
Q8	1.00	24.254	0.99999
Q9	0.50	29.931	0.99999
Q10	0.50	5.9405	0.99999
Q11	0.25	-1.63E-10	0.99991

With the final design of the bending stress phase, a repeated look at the gravitational analysis is performed as well. This allows for an inspection of the deflection of the redesigned structure under gravitational loads. When analyzed, the design of the structure from the bending stress phase deflects 0.2638 in. at the tip as compared to 2.12 in. from the initial design of the gravitational analysis. The structure is designed to be more lightweight and structurally efficient and tailored for aerodynamic loads which it may encounter.

3.4 Use of the Final Design for Fully and Half Deflected Cases

The final design chosen for the structure comes from the design of the bending stress phase that evolved from the successive design approach of the flat case. The design consists of Aluminum Alloy 7075 T651 for the binary, quaternary, and ground links and a plain carbon and low alloy steel for the bracket links. The radius and cross sectional height of each binary and quaternary link, respectively, are tailored to reduce structural weight and increase strength at certain sections. A reduction in gravitational deflection and deflection due to applied loads is achieved from the redesign of the mechanism. This final design is used for the analysis of the fully and half deflected cases. ANSYS models are created for both positions where materials, real constants, and cross sections are set in the models for the binary, quaternary, bracket, and ground links. Gravitational and combined aerodynamic and gravitational analyses are performed for both the fully and half deflected cases. ANSYS is used to determine the deflection of the structures and investigate the maximum axial stresses. The results of the fully and half deflected tests are discussed in the following.

Final Design Applied to Fully Deflected Case

Once the gravity loads are applied to the fully deflected case of the final design, a displacement of 0.226 in. is experienced. Figure 3.6 shows the ANSYS plot of the nodal displacement of the fully deflected case under gravitational loads. The maximum axial stress is located in binary link member B1 as shown in Figure 3.7. There is a maximum stress of 853.8 psi in B1 which is lower than the ultimate tensile strength of 82,700 psi of the Aluminum Alloy 7075 T651 material. The binary links will not fail from the tensile load of the weight of the structure alone.

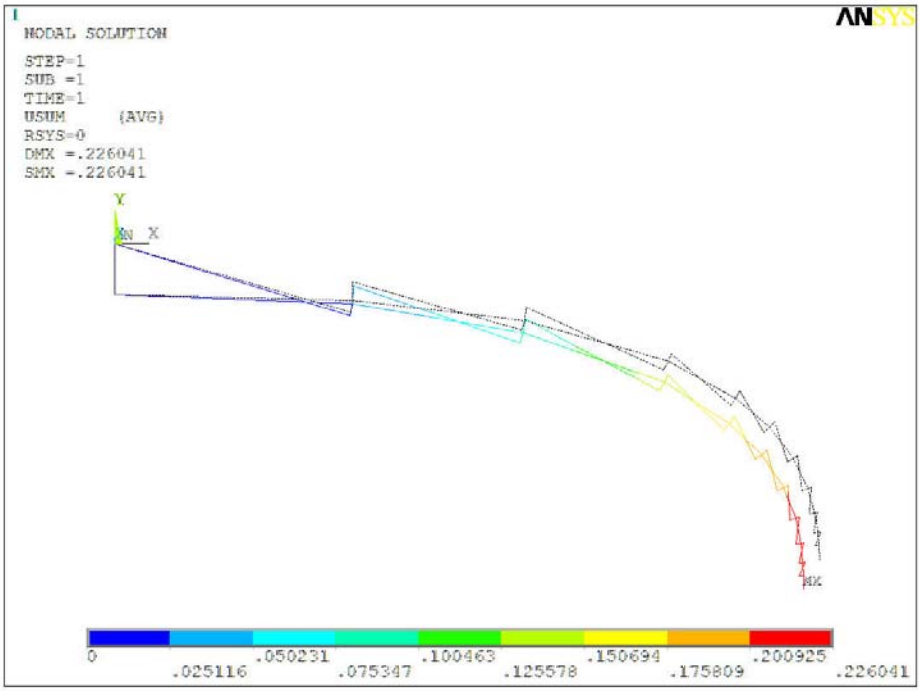

Figure 3.6: A plot of the ANSYS nodal displacements for the fully deflected gravity load case.

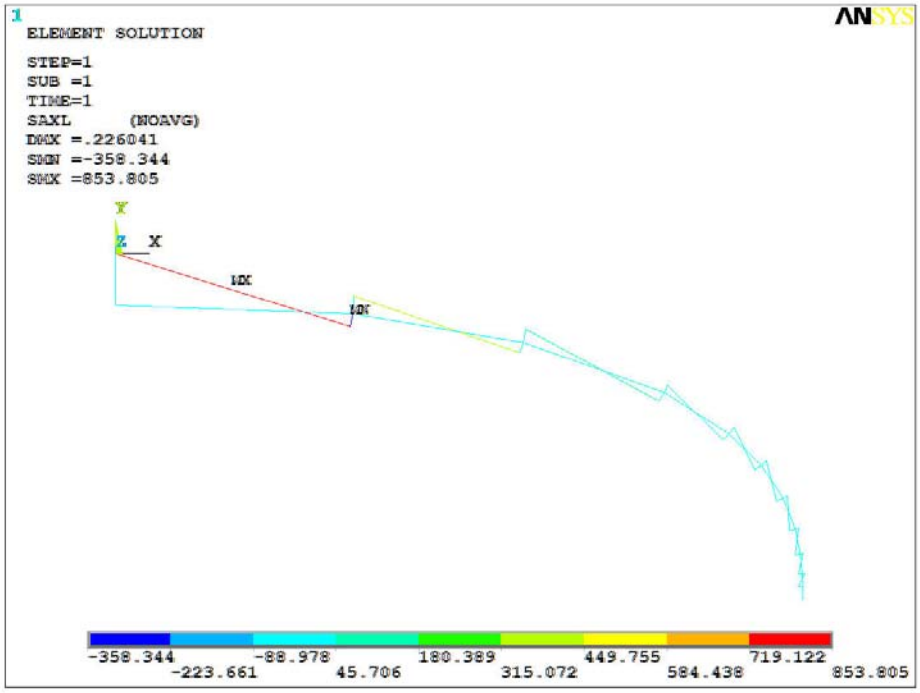

Figure 3.7: An ANSYS axial stress plot of the fully deflected case.

With the applied aerodynamic and gravitational loads, the final design of the fully deflected structure has a displacement of 1.269 in. An ANSYS plot of the deflection is shown in Figure 3.8 where the maximum displacement occurs at the tip of the structure. The maximum bending stress determined from the ANSYS results is in the first quaternary link Q1. It experiences a bending stress of 5053.7 psi. With the calculated maximum bending stress of 7815.6 psi, the factor of safety is equated to 14.5. This factor of safety is not lower than the allowed 1.5. The binary link which receives the largest axial stress of 5271.9 psi is link B1. Dividing this ultimate stress by a factor of 1.5 calculates to a limit stress of 3514.6 psi. The buckling margin of safety is computed to be 1.43. This low and positive margin of safety proves the structure is lightweight and will not buckle under the applied loads. From the analysis of the fully deflected case, it is shown that the structure is efficiently designed to be lightweight and strong enough to withstand the loads at it fully deflected position.

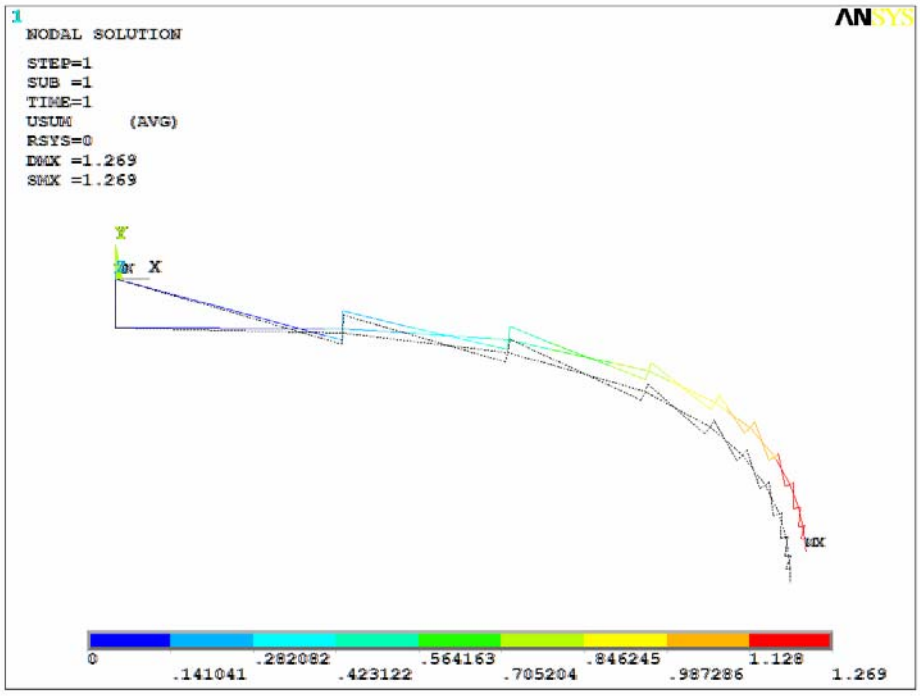

Figure 3.8: An ANSYS deformation plot for the fully deflected applied and gravity load case.

Final Design Applied to Half Deflected Case

The final design is also analyzed in its half deflected case with gravitational loads applied to the model. A 0.253 in. maximum displacement at the tip of the structure occurs due to its own weight. Figure 3.9 shows an ANSYS plot of the nodal displacement of the structure. A maximum axial stress of 875.5 psi occurs at binary link B1. This is illustrated in the axial stress ANSYS plot of Figure 3.10. This maximum stress does not approach the ultimate tensile strength of 82,700 psi of the Aluminum Ally 7075 T651. When comparing the two, the structure does not fail from excessive tension of the highest stressed member.

The predicted aerodynamic loads and gravitational loads are also applied to the half deflected model. The model experiences a maximum displacement of 1.712 in. at the tip of the structure as illustrated in Figure 3.11. Also, according to the ANSYS model, a maximum bending stress of 6305.0 psi occurs at the quaternary link Q1. With a maximum bending stress of 7815.6 psi, the factor of safety for the highest stressed member is 11.6. This factor of safety is higher than the minimum 1.5. The binary link member that has the highest axial stress is B1. It has an axial stress of 6326.6 psi that is divided by 1.5 to achieve a limit stress of 4217.7 psi. The calculated buckling margin of safety for this link is 1.02. Again, this is a low and positive margin of safety proving that the structure is lightweight and structurally effective. From the complete analysis of the final design of the half deflected case, it is shown analytically that the structure is efficient structurally and both lightweight and has high strength.

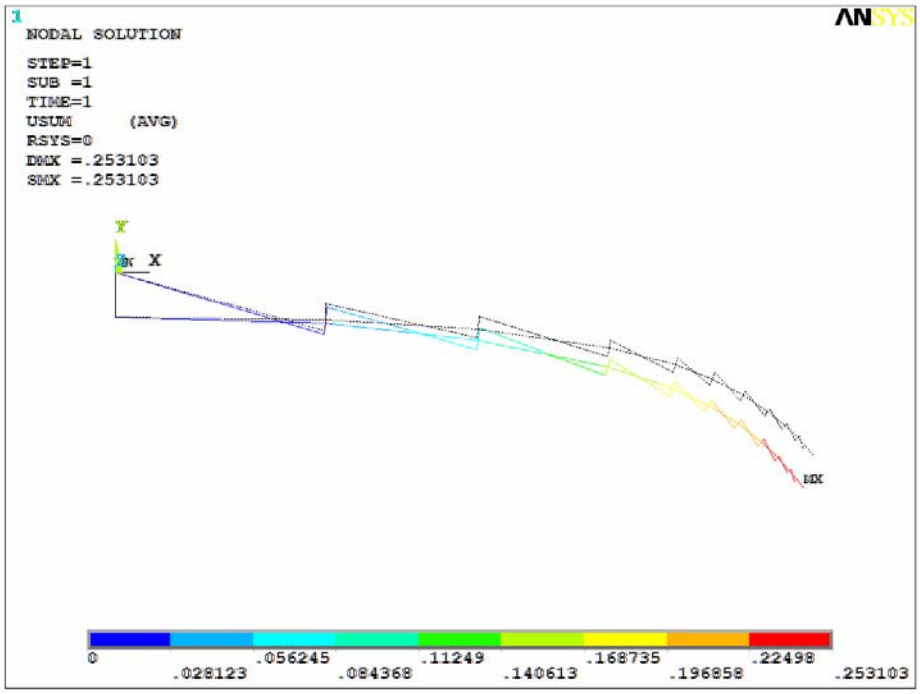

Figure 3.9: A plot of the ANSYS nodal displacements for the half deflected gravity load case.

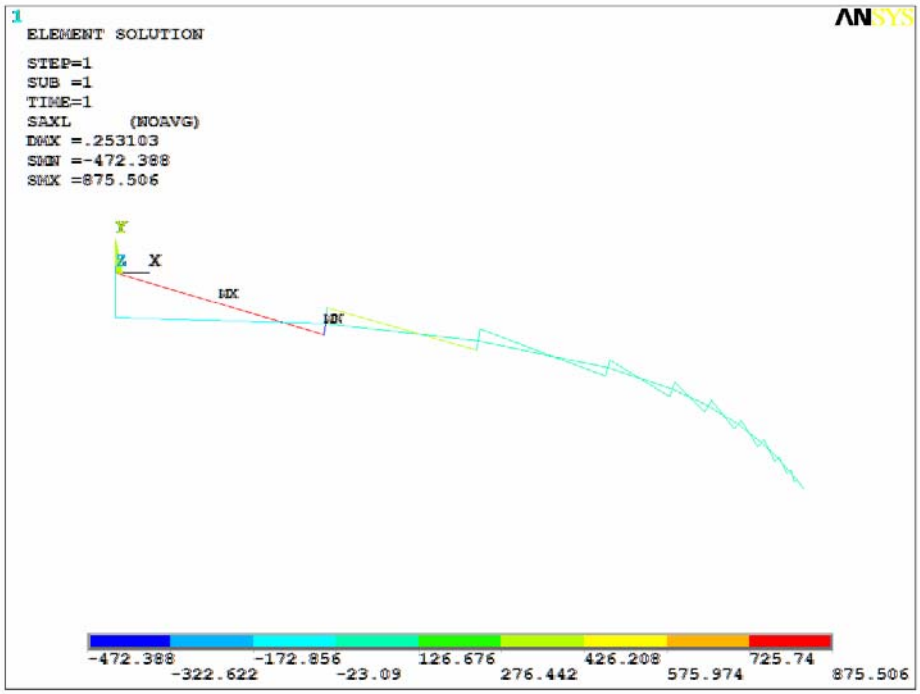

Figure 3.10: An ANSYS axial stress plot of the half deflected case.

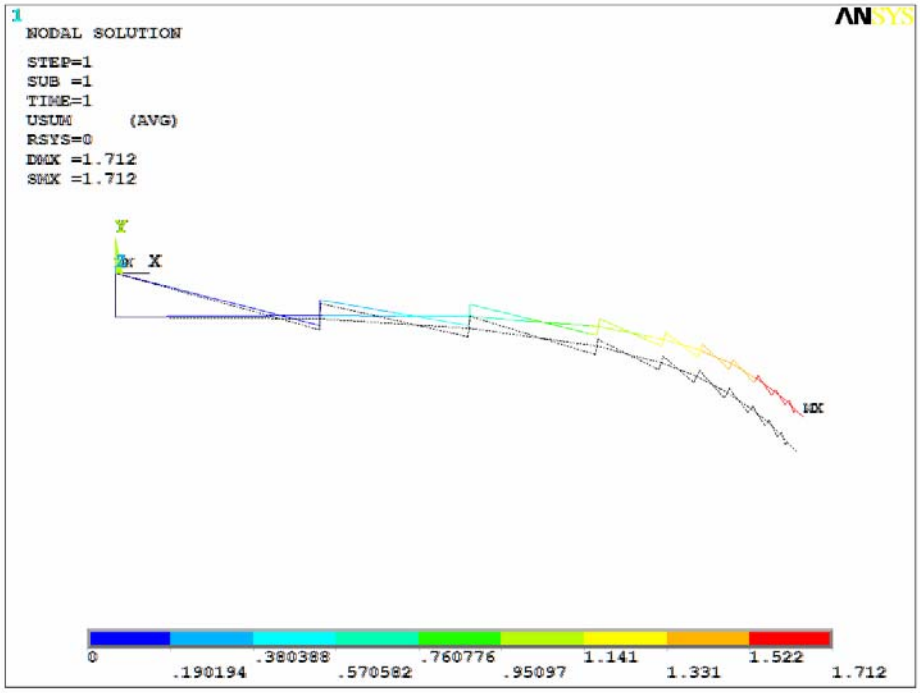

Figure 3.11: An ANSYS plot of the nodal displacement for the half deflected applied and gravity load case.

3.5 Two-Dimensional ANSYS Model Verification Calculations

Calculations are preformed in MATLAB in order to check the results which are given from the ANSYS models. For the calculations, the first section of the flat case model with an applied aerodynamic load at the joint and no gravity loads is taken into account. A diagram of the boundary conditions and an applied load of 105.5 lbf for the first section is shown in Figure 3.12. There are four nodes which define the structure. Element 1 is the quaternary link that is made up of nodes 1 and 2, nodes 2 and 3 define the bracket link of element 2, and the binary link of element 3 is made up of nodes 3 and 4. The aerodynamic load is applied to node 2. For the ANSYS model, there is also and aerodynamic load at node 1, but this was not taken into account for this approximation. That load is also being eliminated from the calculations since that applied force is at node 1 which has a fixed boundary condition along with node 4.

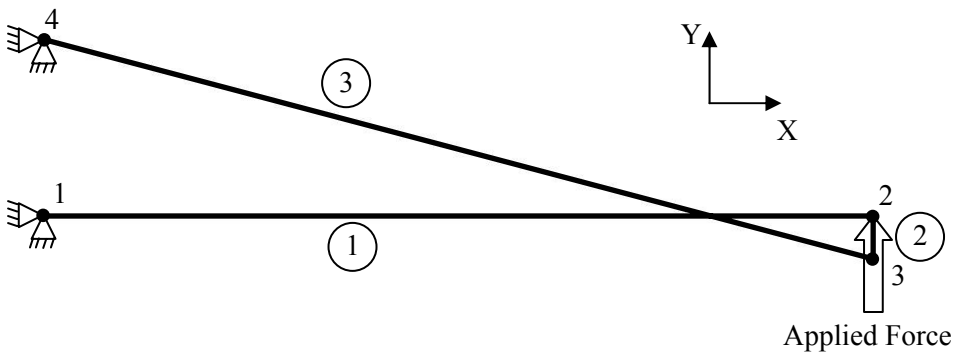

Figure 3.12: An illustration of Section 1 to be modeled.

Element 1, the quaternary link, is treated as a Timoshenko beam to account for the two translational and rotational degrees-of-freedom of the ANSYS model. The beam is allowed to stretch as well as bend. Element 2, the bracket link, is also represented as a Timoshenko beam. Figure 3.13 shows a typical Timoshenko beam element numbered *r* in its local coordinate system $(\hat{x}, \hat{y})$ along with its translational (*u,v*) and rotational (θ_z) degrees-of-freedom at nodes *i* and *j*. The applied forces *P* and *Q* at the nodes in the $\hat{x}$ and $\hat{y}$ directions, respectively, are also shown in the diagram. The property A_r is the cross sectional area, E_r is the elastic modulus, and L_r is the length of each element *r*. The binary link, element 3, is modeled as a rod element as illustrated in Figure 3.14. It has translational degrees-of-freedom (*u,v*) in the $\hat{x}$ and $\hat{y}$ directions, respectively. The applied forces *P* and *Q* occur at the nodes *i* and *j* (Cook *et al*, 2002).

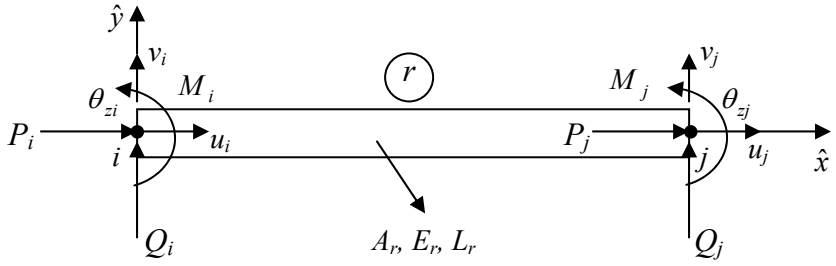

Figure 3.13: The nodal degrees-of-freedom and applied forces and moments of a beam element.

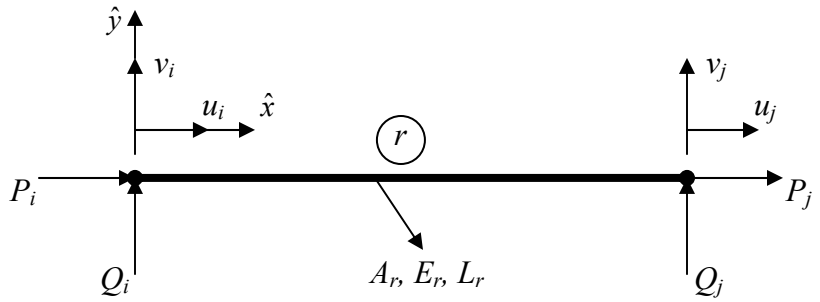

Figure 3.14: The nodal degrees-of-freedom and applied forces of a bar element.

The stiffness matrix for the Timoshenko beam of elements 1 and 2 is as follows (Cook *et al*, 2002),

$$\left[\hat{k}_r\right]=\begin{bmatrix} X & 0 & 0 & -X & 0 & 0 \\ 0 & Y_1 & Y_2 & 0 & -Y_1 & Y_2 \\ 0 & Y_2 & Y_3 & 0 & -Y_2 & Y_4 \\ -X & 0 & 0 & X & 0 & 0 \\ 0 & -Y_1 & -Y_2 & 0 & Y_1 & -Y_2 \\ 0 & Y_2 & Y_4 & 0 & -Y_2 & Y_3 \end{bmatrix}\begin{matrix} \hat{u}_i \\ \hat{v}_i \\ \hat{\theta}_{zi} \\ \hat{u}_j \\ \hat{v}_j \\ \hat{\theta}_{zj} \end{matrix} \qquad 3.5$$

where

$$X=\frac{A_r E_r}{L_r} \qquad Y_1=\frac{12E_r I_{zr}}{(1+\phi_y)L_r{}^3} \qquad Y_2=\frac{6E_r I_{zr}}{(1+\phi_y)L_r{}^2}$$

$$Y_3=\frac{(4+\phi_y)E_r I_{zr}}{(1+\phi_y)L_r} \qquad Y_4=\frac{(2-\phi_y)E_r I_{zr}}{(1+\phi_y)L_r} \qquad \phi_y=\frac{12E_r I_{zr}k_y}{A_r G_r L_r{}^2} \qquad 3.6\text{ - }11$$

and k_y is the shear deformation constant in the y direction which equals 1.2 for solid rectangular cross sections. The shear modulus is G_y, and the area moment of inertia for each element is represented by I_{zr}. The local coordinate system of element 1 lies with the global coordinate system (X,Y). So, $\left[k_1\right]=\left[\hat{k}_1\right]$. However, for element 2, a transformation matrix has to be used (Logan, 2002),

$$[T_2]=\begin{bmatrix} C\alpha & S\alpha & 0 & 0 & 0 & 0 \\ -S\alpha & C\alpha & 0 & 0 & 0 & 0 \\ 0 & 0 & 1 & 0 & 0 & 0 \\ 0 & 0 & 0 & C\alpha & S\alpha & 0 \\ 0 & 0 & 0 & -S\alpha & C\alpha & 0 \\ 0 & 0 & 0 & 0 & 0 & 1 \end{bmatrix} \begin{matrix} u_i \\ v_i \\ \theta_{zi} \\ u_j \\ v_j \\ \theta_{zj} \end{matrix} \qquad 3.12$$

where α is the angle of the element from the global horizontal, X. In this case, the angle α equals 90 degrees. Using this transformation matrix in the following equation allows for the local stiffness matrix of element 2 to be translated in terms of the global system (Logan, 2002),

$$[k_r]=[T_r]^T[\hat{k}_r][T_r] \qquad 3.13$$

For element 2, the stiffness matrix for a rod is as follows (Logan, 2002),

$$[\hat{k}_r]=\frac{A_r E_r}{L_r}\begin{bmatrix} 1 & 0 & -1 & 0 \\ 0 & 0 & 0 & 0 \\ -1 & 0 & 1 & 0 \\ 0 & 0 & 0 & 0 \end{bmatrix} \begin{matrix} \hat{u}_i \\ \hat{v}_i \\ \hat{u}_j \\ \hat{v}_j \end{matrix} \qquad 3.14$$

where A_r, E_r, and L_r are the cross sectional area, Young's modulus, and length of the rod, respectively. The element number r equals 2. This rod element also has to be transformed from its local coordinate system to the global. A transformation matrix similar to that of 3.12 has to be used. The matrix for this element is (Logan, 2002),

$$[T_3]=\begin{bmatrix} C\alpha & S\alpha & 0 & 0 \\ -S\alpha & C\alpha & 0 & 0 \\ 0 & 0 & C\alpha & S\alpha \\ 0 & 0 & -S\alpha & C\alpha \end{bmatrix} \begin{matrix} u_i \\ v_i \\ u_j \\ v_j \end{matrix} \qquad 3.15$$

where the angle α equals about 14.9 degrees. Similar to the bracket link, in order to transform the stiffness matrix from its local form of Equation 3.14 to a global form, Equation 3.13 is used. The stiffness matrix of the binary link does not have any rotational degrees-of-freedom.

Since global equations for each element are defined, the 12 x 12 global stiffness matrix is assembled. This matrix is used in the global nodal forces equation,

$$[F]=[K][d] \tag{3.16}$$

where,

$$[F]=\begin{bmatrix} P_1 & Q_1 & M_1 & P_2 & Q_2 & M_2 & P_3 & Q_3 & M_3 & P_4 & Q_4 & M_4 \end{bmatrix}^T \tag{3.17}$$

and,

$$[d]=\begin{bmatrix} u_1 & v_1 & \theta_{z1} & u_2 & v_2 & \theta_{z2} & u_3 & v_3 & \theta_{z3} & u_4 & v_4 & \theta_{z4} \end{bmatrix}^T \tag{3.18}$$

The *M* term identifies an applied moment. With these parameters described, the global stiffness matrix is assembled as such,

$$[K]=\begin{bmatrix}
\multicolumn{3}{c}{\multirow{3}{*}{$[k_1]_{6x6}$}} & & & & \multicolumn{3}{c}{\multirow{3}{*}{$[k_2]_{6x6}$}} & & & & \\
 & & & & & & & & & & & & \\
 & & & & & & & & & & & & \\
0 & 0 & 0 & & & & & & & 0 & 0 & 0 & u_3 \\
0 & 0 & 0 & & & & \multicolumn{2}{c}{$[k_3]_1$ 2x2} & & 0 & 0 & 0 & v_3 \\
0 & 0 & 0 & & & & & & & 0 & 0 & 0 & θ_{z3} \\
0 & 0 & 0 & 0 & 0 & 0 & \multicolumn{2}{c}{$[k_3]_3$ 2x2} & 0 & \multicolumn{2}{c}{$[k_3]_4$ 2x2} & 0 & u_4 \\
0 & 0 & 0 & 0 & 0 & 0 & & & 0 & & & 0 & v_4 \\
0 & 0 & 0 & 0 & 0 & 0 & 0 & 0 & 0 & 0 & 0 & 0 & θ_{z4}
\end{bmatrix} \tag{3.19}$$

This completes the parameters need for the global nodal forces equation, Equation 3.16. With these factors determined, the direct stiffness method with partitioned matrices is used to first find the nodal displacements [*d*]. The equation for partitioned matrices is (Cook *et al*, 2002),

$$\begin{bmatrix} K_{pp} & K_{pu} \\ K_{up} & K_{uu} \end{bmatrix} \begin{bmatrix} [d_p] \\ [d_u] \end{bmatrix} = \begin{bmatrix} [F_p] \\ [F_u] \end{bmatrix} \tag{3.20}$$

where $[d_p]$ and $[F_p]$ are the prescribed displacements and forces and $[d_u]$ and $[F_u]$ are the unknown displacements and forces. The first equation formed from 3.20 is used to solve for reaction forces,

$$[K_{pp}][d_p] + [K_{pu}][d_u] = [F_p] \tag{3.21}$$

The second equation of 3.20 is solved first for the nodal displacements,

$$[K_{up}][d_p] + [K_{uu}][d_u] = [F_u] \tag{3.22}$$

where the prescribed displacements $[d_p]$ are the known boundary conditions of the problem. In this case, nodes 1 and 4 are fixed, therefore, all degrees-of-freedom for those nodes are zero. That makes the prescribed forces $[F_p]$ equal to the reaction forces and moments of nodes 1 and 4. The unknown displacements are for the nodes we want to equate. This makes $[d_u]$ the translations and rotations for nodes 2 and 3, and $[F_u]$ the applied forces and moments of nodes 2 and 3. These are shown in Equations 3.23 – 26,

$$\begin{aligned} [d_p] &= [u_1 \quad v_1 \quad \theta_{z1} \quad u_4 \quad v_4 \quad \theta_{z4}]^T & [F_p] &= [P_1 \quad Q_1 \quad M_1 \quad P_4 \quad Q_4 \quad M_4]^T \\ [d_u] &= [u_2 \quad v_2 \quad \theta_{z2} \quad u_3 \quad v_3 \quad \theta_{3_4}]^T & [F_u] &= [P_2 \quad Q_2 \quad M_2 \quad P_3 \quad Q_3 \quad M_3]^T \end{aligned} \tag{3.23 - 26}$$

The global stiffness matrix is partitioned according to the prescribed and unknown parameters dictated. When solving Equation 3.22, the prescribed displacements equal zero making the equation to solve for the displacements of nodes 2 and 3,

$$[d_u] = [K_{uu}]^{-1}[F_u] \tag{3.27}$$

where

$$[F_u] = [0 \quad 105.5 \quad 0 \quad 0 \quad 0 \quad 0]^T \text{ lbf} \tag{3.28}$$

and the resulting displacements equal,

$$[d_u] = [1.5258\text{e-}4 \quad 0.2787\text{e-}1 \quad 0.18495\text{e-}2 \quad 0.4253\text{e-}2 \quad 0.2784\text{e-}1 \quad 0.3206\text{e-}2]^T \text{ in} \quad 3.29$$

With the unknown displacements $[d_u]$ determined and $[d_p]$ equal to zero, Equation 3.21 is directly solved for the reactions. The resulting reaction forces and moments are,

$$[F_p] = [-314.46 \quad -22.054 \quad -1006.8 \quad 314.46 \quad -83.483 \quad 0]^T \text{ lbf} \quad 3.30$$

Another calculation that is performed is aimed at determining the axial stress of the binary link. In order to accomplish this, the global displacements at nodes 3 and 4 associated with element 3 are transformed from global to the local coordinate system. The transformation matrix is shown in the following equation,

$$\begin{bmatrix} \hat{u}_3 \\ \hat{v}_3 \\ \hat{u}_4 \\ \hat{v}_4 \end{bmatrix} = \begin{bmatrix} C\alpha & S\alpha & 0 & 0 & 0 & 0 \\ -S\alpha & C\alpha & 0 & 0 & 0 & 0 \\ 0 & 0 & 0 & C\alpha & S\alpha & 0 \\ 0 & 0 & 0 & -S\alpha & C\alpha & 0 \end{bmatrix} \begin{bmatrix} u_3 \\ v_3 \\ \theta_{z3} \\ u_4 \\ v_4 \\ \theta_{z4} \end{bmatrix} \quad 3.31$$

Once the local displacements are found, the following equation is used to find the local forces in the member,

$$\begin{bmatrix} \hat{p}_3 \\ \hat{q}_3 \\ \hat{p}_4 \\ \hat{q}_4 \end{bmatrix} = [\hat{k}_3] \begin{bmatrix} \hat{u}_3 \\ \hat{v}_3 \\ \hat{u}_4 \\ \hat{v}_4 \end{bmatrix} \quad 3.32$$

From this equation, the local forces in the binary link are equated to be,

$$[\hat{f}] = [325.35 \quad 0 \quad -325.35 \quad 0]^T \text{ lbf} \quad 3.33$$

The stress in the third member is calculated from ,

$$\sigma_3 = \frac{f}{A_3} \tag{3.34}$$

where A_3 is the cross sectional area of the circular rod element. With a cross sectional area of 0.2827 in^2, a compressive stress of 1150.69 psi is determined.

The nodal displacement, force, and stress values from the calculations are compared to a similar model set up in ANSYS. The ANSYS model has the same boundary conditions and applied loads as shown in Figure 3.12. It is the same model used for the final design of the flat case with all the sections following the first being deleted along with the gravity load and the applied load to the fixed node of node 1. This allows for a comparison of like models with the hand calculations and ANSYS, and it also varies little from the actual analysis performed on the first section of the structure. The elements, real constants, and material properties are the same as the final design of the flat case and the calculations performed. When solved, Figure 3.15 shows an illustration of the nodal displacement of the structure.

Summary comparison of the ANSYS model and verification calculations are presented in Tables 3.8 – 9. As shown from the tables, the ANSYS model is verified to be accurate for nodal displacements, rotations, forces, and moments with a less than 0.04 percent difference. The resulting force in binary member from ANSYS is 325.28 lbf. Compared to the calculation of 325.35 lbf, this makes gives a percent difference of 0.021 for the member force. The ANSYS model gives a compressive axial member stress of 1150.5 psi. The calculation of this stress gives 1150.69 psi making a percent difference of 0.016.

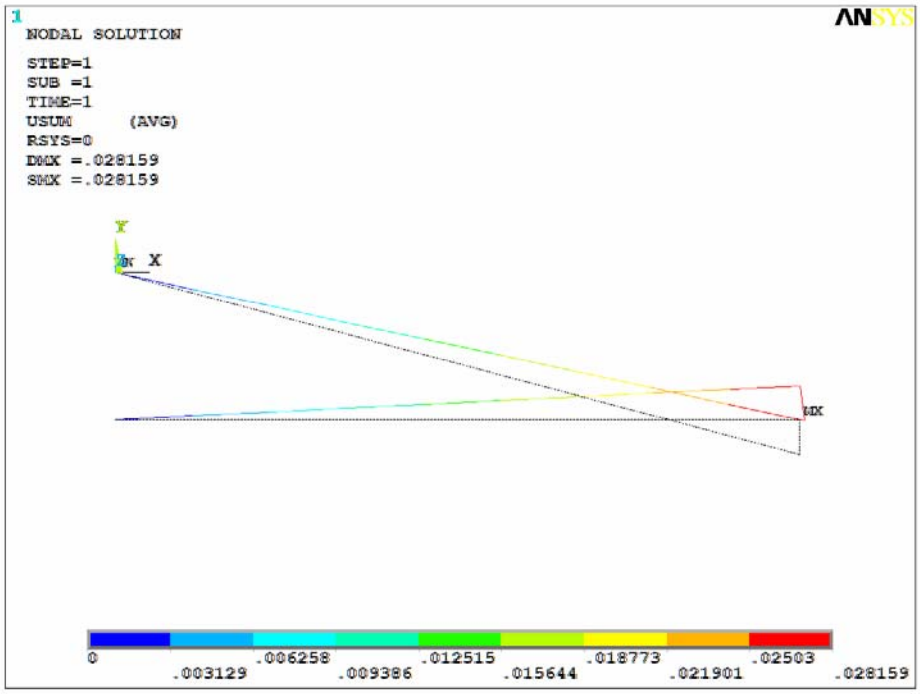

Figure 3.15: An illustration of the deformation of the ANSYS model of Section 1 under the applied load.

Table 3.8: Summary of the difference between the nodal displacements and rotations of the calculations and ANSYS model.

Node, *n*	**Displacement and Rotational Nodal Solutions** $[u_n \quad v_n \quad \theta_{zn}]$			
	[*d*]	**Calculations**	**ANSYS Model**	**% Difference**
1	u_1	0	0	0
	v_1	0	0	0
	θ_{z1}	0	0	0
2	u_2	1.5258e-4	1.5254e-4	0.026
	v_2	0.2787e-1	0.2787e-1	0.007
	θ_{z2}	0.18495e-2	0.18494e-2	0.006
3	u_3	0.4253e-2	0.4254e-2	0.037
	v_3	0.2784e-1	0.2784e-1	0.006
	θ_{z3}	0.3206e-2	0.3205e-2	0.013
4	u_4	0	0	0
	v_4	0	0	0
	θ_{z4}	0	0	0

Table 3.9: Summary of the difference between the nodal forces and moments of the calculations and ANSYS model.

Node, *n*	**Force and Moment Nodal Solutions** $[P_n \quad Q_n \quad M_n]$			
	[*F*]	**Calculations**	**ANSYS Model**	**% Difference**
1	P_1	-314.46	-314.38	0.024
	Q_1	-22.054	-22.056	0.011
	M_1	-1006.8	-1006.8	0.003
4	P_4	314.46	314.38	0.024
	Q_4	-83.483	-83.483	0.003
	M_4	0	0	0

3.6 Chapter Summary

A two-dimensional structural analysis is performed on the kinematic mechanism using ANSYS. The structure is lightened and low strength-to-weight materials are determined from the gravitational study. The binary, quaternary, and ground links are made of Aluminum Alloy 7075 T651 and the bracket links are made of a plain carbon and low alloy steel. From the aerodynamic and gravitational loads analysis, the binary links are designed to withstand buckling and the links are more tailored to the sections of the wing in order to reduce weight. The quaternary links are also redesigned from this analysis to endure bending stresses and they are tailored to the wing sections as well. Verification calculations are performed on a simplified ANSYS model of the first section of the structure. The calculations confirm the results of ANSYS with very low percent differences between the model and the calculations. The final design determined from the two-dimensional analysis is used for an investigation of the three-dimensional tests in the next chapter.

Chapter 4

Three-Dimensional Structural Analysis of the Mechanism

A 3-D model is created and an analysis is performed in ANSYS in order to investigate the stiffness of the quaternary links. There is a possibility of using the quaternary links as the spar of the morphing HECS wing as long as it is rigid enough and placed correctly. The mechanism and rib locations of the wing are modeled at the flat position in 3-D based off the resulting design from the 2-D analysis. The torsion and bending effects of the mechanism are investigated under a static pressure distribution obtained from Johnston's aerodynamic data. This distribution is applied to the rib sections and transmitted to the mechanism. The results are discussed along with redesign suggestions based on those results.

4.1 Three-Dimensional ANSYS Model Development

A 3-D model of the mechanism is designed in ANSYS based on the information discovered from the 2-D analysis. The binary, bracket and quaternary links are modeled. The airfoil rib sections are replicated as well in order to translate the distributed aerodynamic loads experienced from the wing to the mechanism. The binary links are represented with a LINK8 3-D spar element. The element has uniaxial tension and compression with three translational degrees-of-freedom at each

node of x, y, and z. This is an accurate representation of the binary link which is a two force member in three-dimensional space. An Aluminum Alloy 7075 T651 material is used for the binary links. All of the links are modeled with circular cross sections since circular rods are used on the second generation model. The radius of the first link is 0.3 in., the second is 0.05 in., and a radius of 0.002 in. is used for all of the remaining links. Real constant sets for the links which specify the cross sectional area as well as circular cross sections that define the radius of each link are also identified. The full design of these binary links and their cross sections is detailed in the 2-D analysis of the mechanism. The binary link elements are created from nodes that are created from keypoints which are plotted from a MATLAB .log file run in ANSYS.

The bracket links are also formed from nodes of a MATLAB .log file that creates keypoints to locate the links. The element type used to create the brackets is a BEAM4 element. This element has six degrees-of-freedom at each node which include x, y, and z translational as well as rotation about the x, y, and z axes. This uniaxial element is an accurate representation of the brackets in 3-D space that is capable of tension, compression, torsion, and bending. A plain carbon and low alloy steel material is used to define the brackets. The same real constant set and rectangular cross section of $h = 0.875$ in. and $b = 0.125$ in. resulting from the 2-D analysis is used for this study.

The quaternary links are represented with a 3-D solid in ANSYS. These solid links are investigated in detail for the 3-D analysis. A SOLID187 element is used since it's a high order three-dimensional, 10 node element. The solid element has three translation degrees-of-freedom at each node in the x, y, and z directions. The displacement of the element has quadratic behavior which is beneficial when dealing with irregular meshes. The solid link sections are assigned with the Aluminum Alloy 7075 T651 material. Some modifications of the height, h, and width, w, of the cross sections are necessary since they were not discovered during the 2-D analysis. From the 2-D analysis, the quaternary links are modeled with a constant width of 3.5 in. This width is too large for the airfoil sections towards the tip of the structure. The quaternary links are redesigned and tailored more as the chord of the rib sections decrease. The heights of the quaternary links at the rib locations have to be adjusted as well. Some of the heights towards the tip of the structure interfered with the location of the joints for the bracket and binary links. This error is not picked up from the 2-D design, but the locations of the revolute joints are not changed in order to ensure the motion of the mechanism and to avoid a redesign of the mechanism for a first hand 3-D analysis as well. A decrease in heights of the quaternary links toward the tip of the mechanism

serves as a reduction of weight as well. Since there are no drastic changes in height, there is no detrimental change to the structural integrity. Table 4.1 shows a summary of the cross section and cross sectional areas of the quaternary links at each rib location. These entries are the heights and widths used to create the tapered volumes of the quaternary links. In order to ensure that bracket links are connected to a node of the solid quaternary links even after meshing, the volumes of the quaternary links are divided along the *y* direction. This division down the middle of the link makes certain that a node is created at the center, where the beam element of the bracket needs to be located. Real constant sets and cross sections are not required for 3-D solids. MATLAB is used to create ANSYS .log files in order to generate keypoints for the overall shape of the quaternary links. The overall shape of the tapered beam sections for each element is formed. However, the quaternary links need to be designed with angled holes so the binary links may pass through. Elliptically shaped areas on the top and bottom areas of the sections are subtracted from overall top and bottom areas. The resulting areas along with the remaining sides of the section are used to create the volume of the solid with a cut out.

Table 4.1: A summary of the redesigned quaternary links.

Rib Section Number	**Quaternary Link Cross Section**		
	***b* (in)**	***h* (in)**	**Area (in^2)**
1	3.5	1.5	5.25
2	3.5	1.5	5.25
3	3.5	1.5	5.25
4	3.0	1.25	3.75
5	3.0	1.25	3.75
6	2.5	1.25	3.125
7	2.5	0.8	2.00
8	2.0	0.6	1.20
9	1.5	0.3	0.45
10	1.5	0.3	0.45
11	1.0	0.25	0.25

The rib sections of the wing are created with .log files generated from MATLAB as well. From these .log files, keypoints and nodes of the airfoils are made at their specified locations near the joining of the quaternary links. With the nodes and keypoints of the bracket, binary, and quaternary links already defined, it is noticed that the structure does not fit within the airfoil sections. So a change in the design of the location of the revolute joints would not be necessary, the thickness of the SD 7032 airfoil is increased by 60 percent. This is justifiable for an initial investigation of the 3-D effects, but would not be for a step towards an accurate physical model of configuration a morphing HECS wing. Figure 4.1 shows an illustration of the standard SD 7032 airfoil as compared to the one with increased maximum thickness. This increase in thickness assures the top and bottom of the structure fit within the ribs. However, for the first binary link, a point along the line within the boundaries of the rib is picked to ground the link. Picking a point along the line can be done since the link is grounded. A fixture can be designed on a physical model to include the modified ground location along the link. As long as the ground is moved along the line link, the correct motion is still assured.

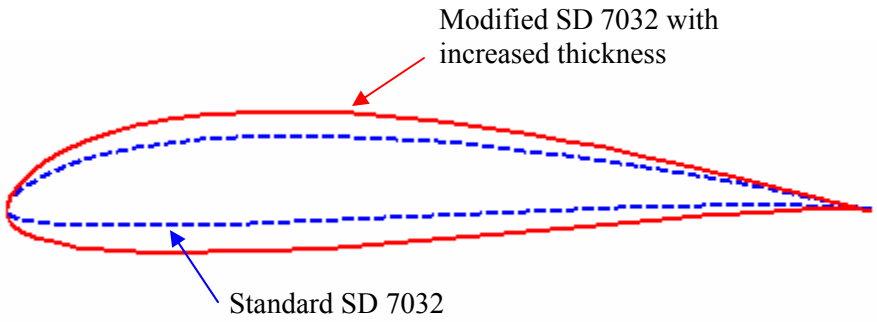

Figure 4.1: A diagram of the standard SD 7032 and its thickness modification for the mechanism.

With the modified SD 7032, the ribs of the structure are generated with BEAM4 elements created from the nodes. The beams are used to create the outside shape of the airfoils. Outside beam sections are diagonally connected by beam elements from the top to bottom at certain nodes creating a truss like structure within airfoil. This provides a structural idealization of stiffeners, webs, and flanges which may be used in the design of an actual rib (Megson, 1972). The rib elements are made with an Aluminum 2014 T6 material which has a weight density of 2.62E-4 lbf-s^2/in^4 and a Young's modulus of 10,500 ksi. The rib sections are used as a means to simulate and transmit a distributed load across the wing to the mechanism without having to model the wing surface.

The wing surface is not modeled in order to simplify the 3-D analysis of the mechanism. To compensate for morphing, in theory, the HECS wing surface can be made with a solid material while a more flexible material is used across the revolute locations. A material may also exist that can be stretched across the entire wing configuration. For morphing, this wing surface material needs to be elastic enough to morph and stiff enough to withstand the loads. Because of these design uncertainties, the wing surface is not modeled for this 3-D analysis.

Fixed zero degree-of-freedom boundary conditions are applied to the root area of the first quaternary link. The node of the first binary link of the structure is also fixed with a zero degree-of-freedom boundary condition. Zero rotational degrees-of-freedom are applied to the nodes where the quaternary and bracket links connect. Assigning these degrees-of-freedom makes sure the 90 degrees between those two links is kept. The predicted aerodynamic pressure is applied to the top of the airfoil sections. The pressure across the chord is applied to the rib beam elements in ANSYS at approximately five evenly spaced sections.

With the elements of the binary, bracket, and rib sections defined and volumes of the quaternary links located, constraint equations must be created on the connecting loads of the solid and beam elements. These equations are required because the beam elements have translational and rotational degrees-of-freedom, while solids and planes have only translational degrees-of-freedom. If the rotational degrees-of-freedom of the beam elements are not transferred to the solids, the beam element essentially acts as a hinge (Cook *et al*, 2002). Figure 4.2 shows an illustration of a beam element attached to a plane element. The illustration shows the different deformations that are experienced with and without constraint equations. The constraint equations can be entered in ANSYS in the following form,

$$C = C_1 L_1 + C_2 L_2 + C_3 L_3 \tag{4.1}$$

where C, C_1, C_2, and C_3 are constant terms. L_1, L_2, and L_3 represent the nodal degree-of-freedom terms whether it is a translational x, y, and z or a rotational θ_x, θ_y, and θ_z. In order to transfer the moment, θ_y, of the beam element to the plane at node two the following equation is used,

$$\tan\theta_{y2} = \frac{W_{z3} - W_{z1}}{bh} \tag{4.2}$$

where W_{z1} and W_{z3} are the displacements of nodes 1 and 3, respectively, in the z direction, and b and h are the distances between the nodes. Using small angles, $\tan\theta_{y2} \approx \theta_{y2}$, the Equation 4.2 can be manipulated in the form of Equation 4.1,

$$0 = W_{z1} - W_{z3} + bh\theta_{y2} \tag{4.3}$$

The coefficient, nodal, and rotational information entered into ANSYS is $C = 0$, $C_1 = 1$ at node 1 and translational W_{z1}, $C_2 = -bh$ at node 2 and rotational θ_{y2}, and $C_3 = -1$ at node 3 and translational W_{z3}.

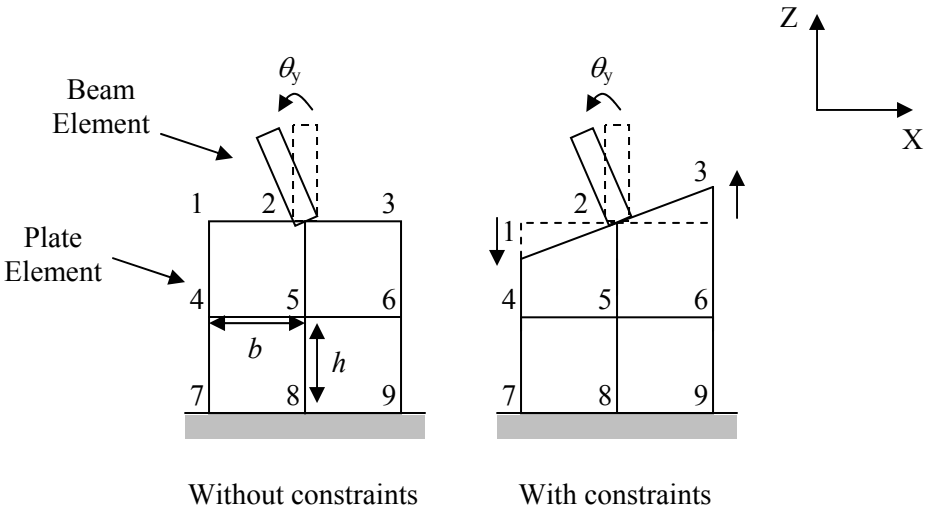

Figure 4.2: An illustration of a beam rotational degree-of-freedom transferred to the translational degrees-of-freedom of a plane element.

The method of the example is used to transfer the rotational degrees-of-freedom of the beam elements of the rib sections to the translational degrees of freedom of the solids. Figure 4.3 shows diagram of a rib section and quaternary link. The beam elements can experience rotation because of the applied aerodynamic pressure. This pressure is greater towards the leading edge and decreases towards the trailing edge. Being able to transfer the rotation of the beam elements is key to analyzing the torsion effects on the quaternary links.

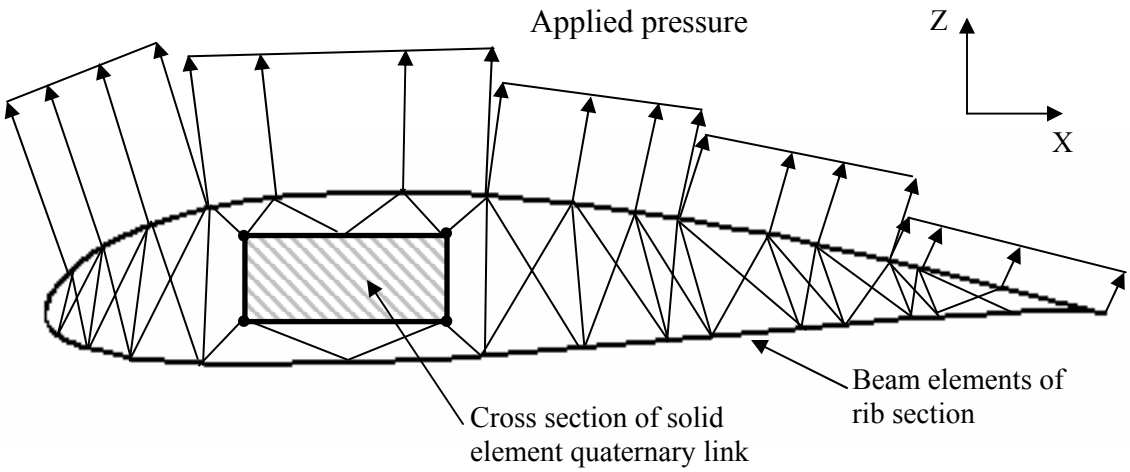

Figure 4.3: A diagram of the attachment of a rib section to a quaternary link with an applied pressure.

A mesh of the quaternary link volumes is created. The volumes are given the material, real constant, and element type attributes of the quaternary links. The mesh is created using the smart size control of a free mesh of the volumes. With the mesh of the volumes generated, the connection of the bracket links and rib sections are still ensured at the nodal locations that were picked on the edge of the shape. A NUMMRG command in ANSYS is used once the mesh is formed to ensure that the constraint equations are kept with the assigned nodal numbers. This command will merge coincidental nodes. Figure 4.4 shows a planform view of the meshed model in ANSYS. Figure 4.5 shows the meshed structures with the applied pressure distribution on the ribs and boundary conditions in an isometric view.

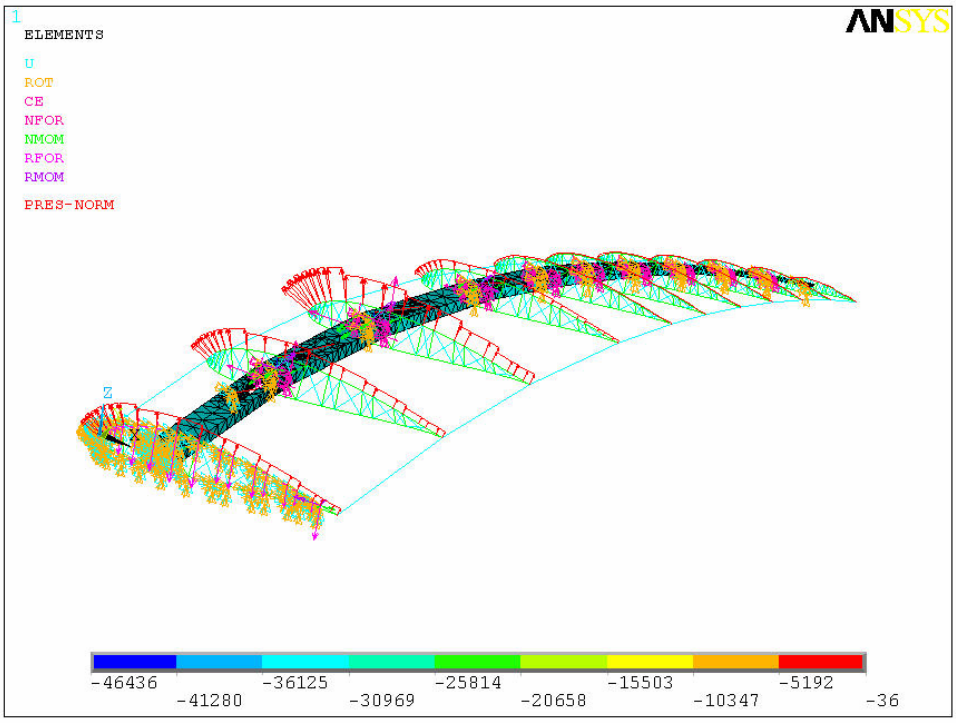

Figure 4.4: An isometric illustration of the applied loads and boundary conditions.

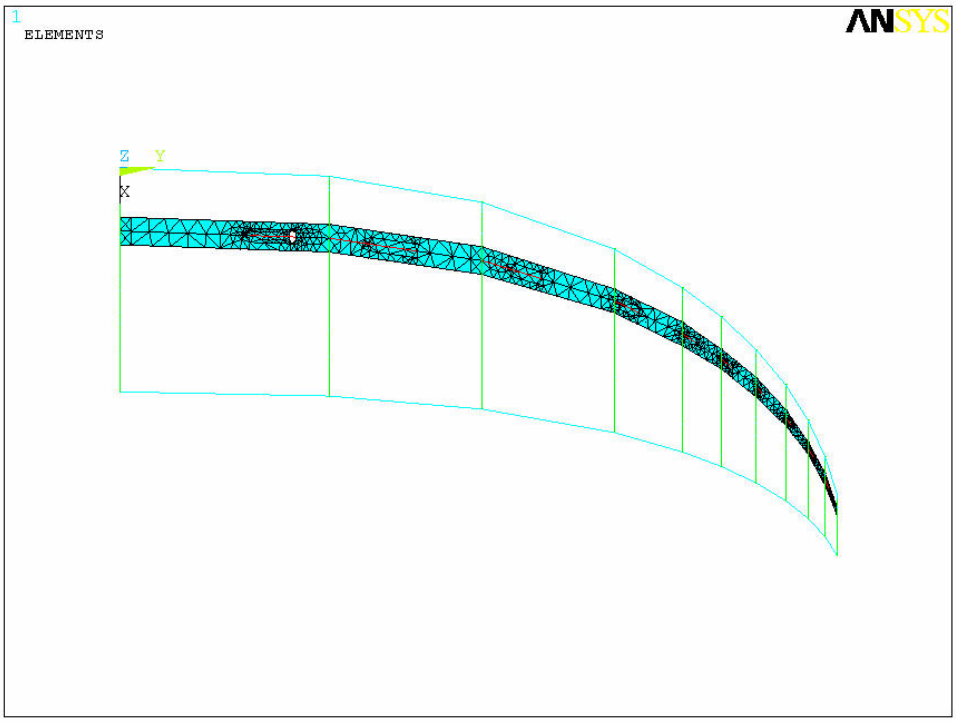

Figure 4.5: A planform view of the structure modeled and meshed in ANSYS with the applied distributed loads.

4.2 Analysis Process

The purpose of the 3-D analysis of the mechanism is to investigate the general characteristics of the structure and make design improvement suggestions. The solid model analysis is carried out using an iterative solution process. The objective of this process is to converge on a value for the maximum principal stress. In ANSYS, the smart sizing control of the meshed volumes of the quaternary links is iterated from a more coarse size setting of six to a fine setting of one. Once an area of concentration is noticed with a fine mesh, nodal mesh refinement along the area is performed.

Smart mesh sizes are set for the volumes of the quaternary links. A resulting deformation and occurrence of the maximum principal stress is shown in Figure 4.6. There are a couple of interesting points about the deformation and stress that have to be understood before further results could have been taken. First, the stress occurs at a node of the point of contact between the quaternary and beam element. These attachment points may be areas of stress concentrations because of the square edges of the quaternary solids. This is equivalent to a point load on the solid resulting in a singularity. With this in mind, it is noted that, intuitively, the stress concentration approaches infinity. This does not necessarily mean a certain value can not be achieved since a square corner or hole can not be practically manufactured. However, it does indicate that a convergence on a particular value may be more difficult. Lastly, the ribs on the trailing edge of the structure deform more than the mechanism solid links. In order to investigate why this is happening, a trial and error method of assigning different modulus of elasticity and cross section geometry for the beam elements internal to the rib structure is performed. From this investigation, it is found that by increasing the cross sectional areas of the internal stiffeners of the beams the deflections occurring at the trailing edge are decreased. Changing the modulus of elasticity does not have as much of a decrease as changing the cross section. A rectangular cross section of $b = 5$ and $h = 20$ is used for the analysis of the mechanism which gives a maximum displacement of 0.170 in. in the positive z direction for the trailing edge of the third rib. This value is in range with some of the deflections of the 2-D analysis. While keeping in mind the issues of the model, mesh iterations are taken using the adapted stiffeners. The stress concentration is to be examined as well as the reasoning of why the ribs deflect in the positive z direction even though that is where the load distribution is the minimum.

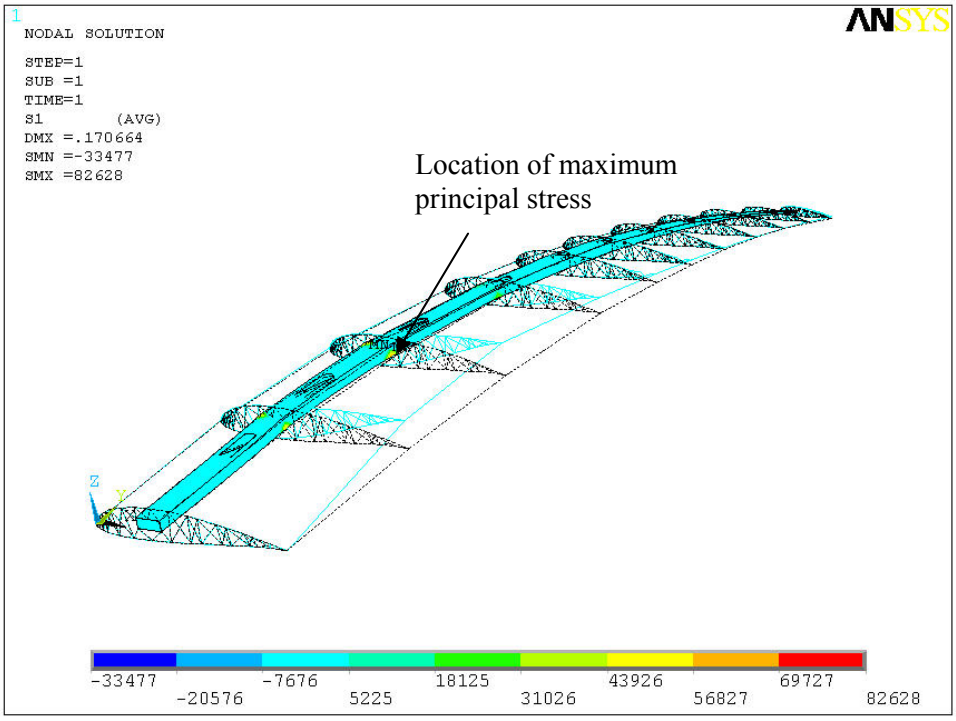

Figure 4.6: An ANSYS plot of a result showing possible stress concentrations and unexpected deformations.

4.3 Discussion of Analysis Results and Redesign Suggestions

From the mesh iterations, it is discovered that there are stress concentration locations at the connecting nodes of the beam and quaternary links. Table 4.2 shows the resulting maximum principle stresses located at the same connecting node as seen in Figure 4.6. A plot of the stresses is shown in Figure 4.7. It is shown that the maximum principal stress does not approach a value. After mesh refinement iterations, the stresses begin to exhibit the behavior of an exponential increase. This behavior indicates a maximum stress of infinity. Since a perfectly square edge or hole can not be machined, some type of maximum stress would exist. However, the material will likely fail before reaching this maximum value. Figure 4.8 shows a plot of the principal stress for the final mesh iteration. From this plot, it can be seen that the beam experiences some rotation which tells that the constraint equations are working properly. However, with the stress concentrations, there needs to be a more realistic method of connecting the ribs to the quaternary links. This may be resolved when the design of the wing begins to be finalized.

Table 4.2: A summary of the maximum principal stresses.

Mesh Iteration	Smart Mesh Size (1 max)	Maximum Principal Stress (psi)
1	8	82627
2	7	83428
3	6	91395
4	5	92934
5	4	91454
6	3	100038
7	2	95990
8	1	122633

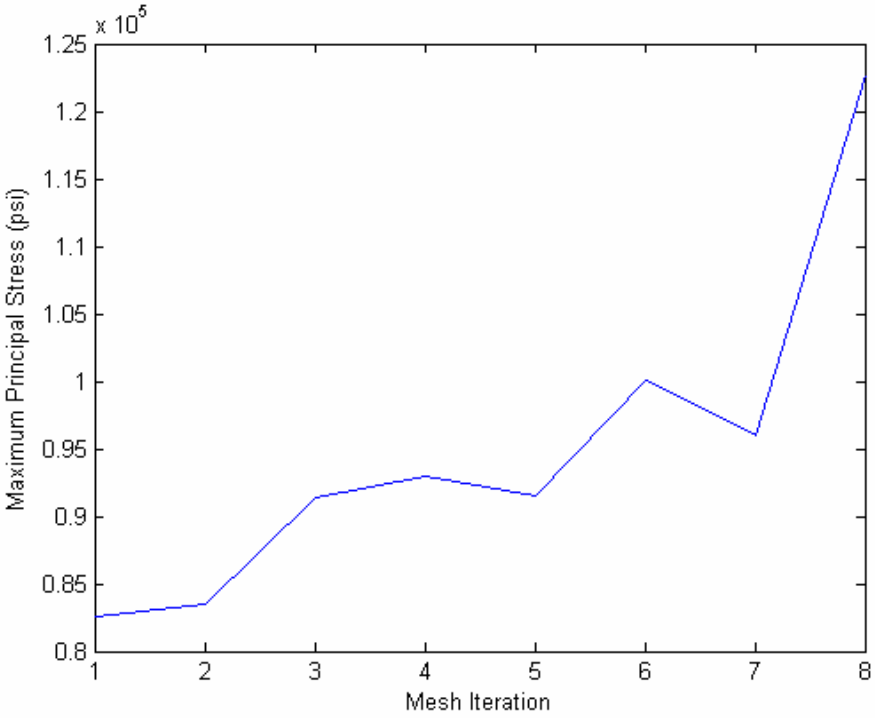

Figure 4.7: A plot of the maximum principal stress after each mesh iteration.

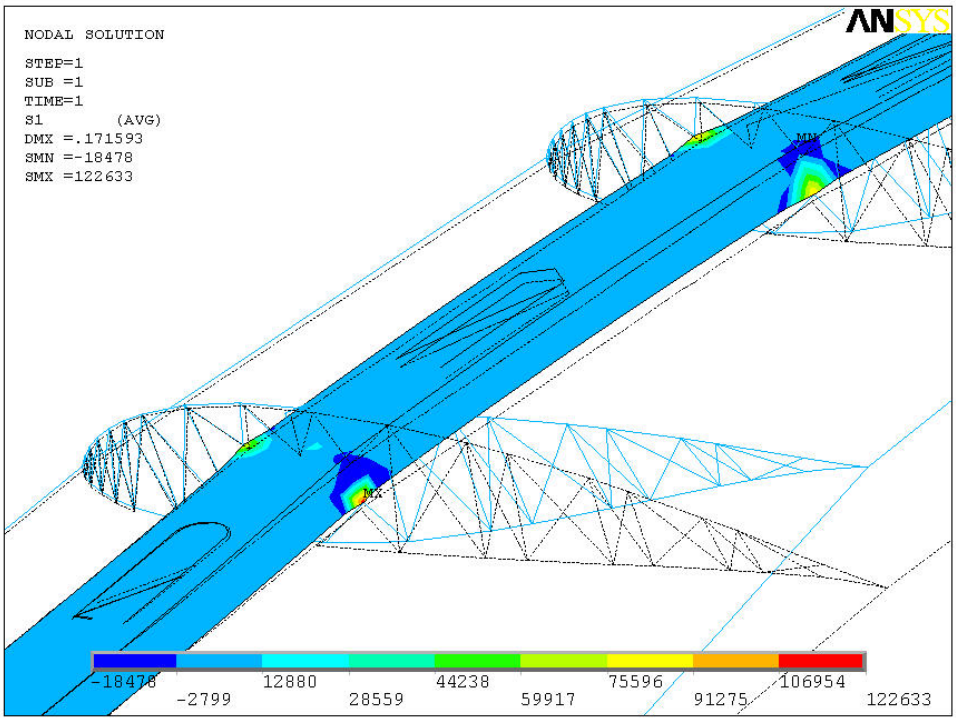

Figure 4.8: Plot of the principal stress for the final mesh iteration.

It is found that the reason the trailing edge of the rib section is deflecting is because the quaternary links of the mechanism are serving as a rigid spar. The moment created along the chord from the mechanism to the trailing edge is greater than the moment created on the leading edge. This has to do with the distance between the locations as well. However, this result does support the design suggestion of the mechanism being the structural support of the wing. With the quaternary links designed to carry enough load, these links can be the spar of the wing. For this analysis, the mechanism is designed around the maximum thickness location at the chord of the wing. A way to decrease the deflection experienced along the trailing edge of the ribs is to move the mechanism back further from the leading edge. This decreases the moment arm created.

4.4 Chapter Summary

A 3-D finite element model of a mechanism to morph the HECS wing is produced. This model affords the opportunity to examine different materials and cross sections of the links, change the location of the holes for the binary links, apply different loads on the airfoil sections, and investigate the structural effects of the applied load on the members of the mechanism. With this model, an idea of how changes in certain aspects of the wing and mechanism can be evaluated in a static sense is shown. From these initial tests of the model, it is shown that the mechanism can serve as a spar for the HECS wing with the correct placing. Stress concentration locations are discovered from the connecting nodes of the solid and beam elements. These concentrations may be reduced by rounding the edges where the quaternary links meet.

Chapter 5

Conclusions

5.1 Brief Summary of Thesis

A structural analysis of the kinematic mechanism designed to morph the HECS wing using aerodynamic loads predicted by Johnston is performed. A successive approach is used to investigate the criteria of the 2-D model. The nodal displacements and force, stress, and buckling of the members is investigated. The 2-D model is created with link and beam elements in ANSYS. Once the material properties, real constants, and cross sections are set for each member, boundary conditions and loads are applied. There are two analysis performed. One evaluates the structure under its own weight. Materials are chosen with high strength-to-weight ratios which lighten the structure as well as decrease its maximum displacement.

The other 2-D analysis has both gravitational loads and Johnson's predicted aerodynamic loads applied to the structure. The binary links are modeled to withstand buckling loads as well as tailored with smaller cross sections for the sections that do not experience high loads. This allows for more reduction of more structural weight. The cross sections of the quaternary links are also tailored from the root to tip of the structure to withstand bending stresses. The sections towards the root proved to need an increase cross section as compared to the ones toward the tip. This is because of the nature of the applied aerodynamic load.

Verification calculations prove the model developed in ANSYS as being accurate. The calculations are performed on the first section of the mechanism alone and without gravity affects. By using a finite element method analysis, the nodal displacements, rotations, forces and moments agree to low percent differences with a maximum of 0.037 percent. This confirms not only the accuracy of the model, but also its representation.

A 3-D finite element model is created of the mechanism and airfoil sections. This model allows for the application of a distributed pressure load on the ribs and translates the effects to the quaternary links of the mechanism. Adjustments can be made on the link members and be analyzed. It is discovered that by locating the mechanism around the maximum thickness location along the chord, the mechanism can provide structural support for the wing. An initial investigation of 3-D influences on the mechanism is possible with this model.

5.2 Contributions

This work contributes a finite element models capable of analyzing the kinematic mechanism which is designed to morph the HECS wing in 2-D and 3-D. In 2-D, The mechanism can be studied at flat, half deflected, and fully deflected morphing locations. This finite element model allows for the redesign of the members of the mechanism once loads are applied. This redesign can in turn decrease the weight of the structural as well as increasing the strength. With results from analysis using these models, another step of creating a better physical model is achieved.

5.3 Future Work

For future work, a physical model of the wing including the mechanism can be made. This model will allow for wind tunnel tests of the structural design which can be fitted with strain gauges. This will not only be a way to test the finite element model, but it will also allow testing of the predicted aerodynamic loads as well. A dynamic analysis of the mechanism as it moves from one position to the next can also be performed. With the structural model designed, equations of motion for the members of the mechanism can be derived. From these equations of motion, the kinematic mechanism can be evaluated dynamically. A vibration analysis of the wing structure

with the mechanism would also be beneficial. The effects that the mechanism has on the mode shapes of the wing may be interesting.

Bibliography

Cone, C.D., "The Aerodynamic Design of Wings with Cambered Span Having Minimum Induced Drag," NASA TR-R-152, 1963.

Cone, C.D., "The Theory of Induced Lift and Minimum Induced Drag on Non-Planar Lifting Systems," NASA TR-R-139, 1962.

Cook, R.D., Malkus, D.S., and Plesha, M.E., Witt, R.J., *Concepts and Applications of Finite Element Analysis*, John Wiley & Sons Inc., New York, New York, 2002.

Curtis, H.D., *Fundamentals of Aircraft Structural Analysis*, WCB/McGraw-Hill, Boston, Massachusetts, 1997.

Davidson, J.B., Chwalowski, P., and Lazos, B.S., "Flight Dynamic Simulation Assessment of a Morphable Hyper-Elliptic Cambered Span Winged Configuration," AIAA Paper 2003-5301, *AIAA Atmospheric Flight Mechanics Conference and Exhibit*, Austin, TX, August 11-14, 2003

Gern, F.H., Inman, D.J., and Kapania, R.K., "Computation of Actuation Power Requirements for Smart Wings with Morphing Airfoils," AIAA Paper 2002-1629, *43rd AIAA/ASME/ASCE/AHS/ASC Structures, Structural Dynamics, and Materials Conference and Exhibit*, Denver, CO, April 22-25, 2002.

Johnston, C.O., Neal, D.A., Wiggins, L.D., Robertshaw, H.H., Mason, W.H., and Inman, D.J., "A Model to Compare the Flight Control Energy Requirements of Morphing and Conventionally Actuated Wings," AIAA Paper 2003-1716, *43rd AIAA/ASME/ASCE/AHS/ASC Structures, Structural Dynamics, and Materials Conference and Exhibit*, Norfolk, VA, April 7-10, 2003.

Logan, D.L., *A First Course in the Finite Element Method*, Brooks/Cole, Pacific Grove, CA, 2002.

Lowson, M.V., "Minimum Induced Drag for Wings with Spanwise Camber," *Journal of Aircraft*, Vol. 27, July, 1990, pp. 627-631.

McGowan, A-M.R., Washburn, A.E., Horta, L.G., Bryant, R.G., Cox, D.E., Siochi, E.J., Padula, S.L., and Holloway, N.M., "Recent Results from NASA's Morphing Project," SPIE Paper 4698-11, *9th Annual International Symposium on Smart Structures and Materials*, San Diego, CA, March 17-21, 2002

Megson, T.H.G., *Aircraft Structures for Engineering Students*, Edward Arnold Ltd., London, 1972.

Norton, R.L., Machine Design An Integrated Approach, Prentice-Hall Inc., Upper Saddle River, New Jersey, 1998.

Pettit, G.W., Robertshaw, H.H., Gern, F.H., and Inman, D.J., "A Model to Evaluate the Aerodynamic Energy Requirements of Active Materials in Morphing Wings," Proceedings of DETC'01, 2001 ASME Design Engineering Technical Conferences, September, 2001.

Prock, B.C., Weisshaar, T.A., and Crossley, W.A., "Morphing Airfoil Shape Change Optimization with Minimum Actuator Energy as an Objective," AIAA Paper 2002-5401, *9th AIAA/ISSMO Symposium on Multidisciplinary Analysis and Optimization*, Atlanta, GA, September 4-6 2002.

Rivello, R.M., *Theory and Analysis of Flight Structures*, Mc-Graw-Hill, Inc., New York, New York, 1969.

Stubbs, M.D., "Kinematic Design and Analysis of a Morphing Wing," Masters Thesis, Virginia Polytechnic Institute & State University, 2003.

Whittier, W.B., "Kinematic Analysis of Tensegrity Structures," Masters Thesis, Virginia Polytechnic Institute & State University, 2002.

Wiggins, L.D., Stubbs, M.D., Johnston, C.J., Robertshaw, H.H., Reinholtz, C.F., and Inman, D.J., "A Design and Aanlysis of a Morphing Hyper-Elliptic Cambered Span (HECS) Wing," AIAA Paper 2004-1885, To be submitted to: *45th AIAA/ASME/ASCE/AHS/ASC Structures, Structural Dynamics & Materials Conference and Exhibit* , Palm Springs, CA, April 19-22, 2004.

Appendix A

Table A.1: Summary of the slenderness ratio for each binary link calculated from Equation 3.2.

Binary Link	Slenderness Ratio
B1	109.6
B2	78.4
B3	67.5
B4	35.2
B5	21.2
B6	18.8
B7	15.6
B8	12.0
B9	9.15
B10	6.60

Vita

Leonard D. Wiggins, III was born to Vivian A. Wiggins and Leonard L. Wiggins, Jr. on November 4, 1979 in Suffolk, VA. Upon graduation from Lakeland High School in Suffolk, VA, Leonard started at Virginia Tech in the summer of 1997 in the ASPIRE summer program for minorities in engineering. Leonard co-oped three terms at Bristol Compressors, Inc. in Bristol, VA during his undergraduate career and worked as an undergraduate researcher at the CIMSS lab at Virginia Tech with the Morphing Wing Program. He completed his Bachelor of Science degree in Mechanical Engineering during the spring of 2002. He began as a graduate researcher at CIMSS with the Morphing Wing Program. Upon completion of his Master of Science degree in Mechanical Engineering during the fall semester of 2003, Leonard is fed up with Blacksburg, VA and the cold weather! He will be going down south to work in New Orleans, LA. Oh yeah, Leonard likes to play basketball, lift weights, and have fun in his free time.